










Phloem iron remodels root development in response to ammonium as the major nitrogen source

Xing Xing Liu ¹, Hai Hua Zhang ¹, Qing Yang Zhu ¹, Jia Yuan Ye ¹, Ya Xin Zhu¹, Xiang Ting Jing ¹, Wen Xin Du ¹, Miao Zhou ¹, Xian Yong Lin¹, Shao Jian Zheng ² & Chong Wei Jin ¹✉

Plants use nitrate and ammonium as major nitrogen (N) sources, each affecting root development through different mechanisms. However, the exact signaling pathways involved in root development are poorly understood. Here, we show that, in *Arabidopsis thaliana*, either disruption of the cell wall-localized ferroxidase LPR2 or a decrease in iron supplementation efficiently alleviates the growth inhibition of primary roots in response to NH_4^+ as the N source. Further study revealed that, compared with nitrate, ammonium led to excess iron accumulation in the apoplast of phloem in an LPR2-dependent manner. Such an aberrant iron accumulation subsequently causes massive callose deposition in the phloem from a resulting burst of reactive oxygen species, which impairs the function of the phloem. Therefore, ammonium attenuates primary root development by insufficiently allocating sucrose to the growth zone. Our results link phloem iron to root morphology in response to environmental cues.

¹State Key Laboratory of Plant Physiology and Biochemistry, College of Natural Resources and Environmental Science, Zhejiang University, Hangzhou 310058, China. ²State Key Laboratory of Plant Physiology and Biochemistry, College of Life Science, Zhejiang University, Hangzhou 310058, China.
✉email: jincw@zju.edu.cn

Nitrogen (N) is the essential nutrient required in the greatest quantity by plants. It is primarily acquired by plant roots in the forms of ammonium (NH_4^+) and nitrate (NO_3^-). Nevertheless, NH_4^+ is notoriously toxic to most plants when present as the only or predominant N source¹, which is not the case for NO_3^- . In fact, NH_4^+ stress is of major importance to the ecology of soils that exhibit higher ammonification than nitrification rates, such as those found in wetlands, including saltmarshes, bogs, mangroves, and fens^{2–4}. In addition, because of highly intensive tillage or waterlogged cultivation methods, many crop plants also suffer long-term NH_4^+ stress induced by the over-application of N fertilizers⁵. Identification of the mechanisms underlying toxicity and detoxification of NH_4^+ in plants is crucial for improving the adaptation of the plants in the presence of NH_4^+ as the primary N source.

Similar to many other abiotic cues, NH_4^+ stress also inhibits the growth of primary roots (PRs); hence, stunted PR growth is recognized as a typical symptom of NH_4^+ toxicity^{6,7}. The uptake of NH_4^+ by roots is the first step affecting cellular NH_4^+ concentration and therefore is an important process affecting NH_4^+ stress in plants. Knocking out NH_4^+ transporters (AMTs) AtAMT1;1, AtAMT1;2, and AtAMT1;3 results in a 90% reduction in NH_4^+ uptake and substantially decreases NH_4^+ sensitivity⁸. The protein kinase AtCIPK23 phosphorylates and inactivates AtAMT1;1 and AtAMT1;2, and thus activation of AtCIPK23 expression by transcription factor AtSTOP1 has been identified as a mechanism for NH_4^+ tolerance^{9,10}. A decrease in NH_4^+ uptake due to enhanced proton extrusion from the resulting activation of H^+ -ATPase has also been shown to be a mechanism for NH_4^+ tolerance^{11,12}.

A high concentration of cellular NH_4^+ also causes a variety of physiological damage in plants, such as disordered pH regulation, excess energy consumption, deficiency of mineral cations, increased oxidative stress, and disruption of hormonal homeostasis^{4,6,13}. Lines of evidence have linked some of these effects to NH_4^+ toxicity. For example, the reaction of the glutamine synthetase GLN2 in shoots over-produces protons, resulting in pH disorder and consequently contributing to NH_4^+ toxicity in the shoots¹⁴; NH_4^+ stress results in excessive production of hormone ethylene, while EIN2- and EIN3-mediated ethylene signaling partly causes NH_4^+ toxicity in shoots^{15,16}. However, these physiological effects are indirectly related, and most of them explain NH_4^+ toxicity in shoots but not in the roots⁶.

Currently, only a few signaling events have been proposed to mediate NH_4^+ -induced PR growth inhibition. A previous study showed that knockout of *VTCL*, which encodes a GDP-mannose pyrophosphorylase, results in greater inhibition of PR growth under NH_4^+ stress, but the underlying mechanism remains unclear¹⁷. Auxin was also suggested to be associated with the NH_4^+ -sensitive phenotype of PRs¹⁸. However, it has been shown that the PR growth of auxin transport mutant *aux1* is similar to that of the wild-type plant under NH_4^+ stress¹⁹, leaving it open as to whether auxin plays a role in NH_4^+ -induced PR growth inhibition. Therefore, the mechanisms, particularly the molecular pathways, underlying the negative impacts of NH_4^+ in PR growth remain largely unknown^{4,6}.

In this work, we screened an Arabidopsis (*Arabidopsis thaliana*) transfer DNA (T-DNA) insertion mutant whose PR growth is insensitive to NH_4^+ stress. The T-DNA insertion in this mutant was annotated in the gene *LOW PHOSPHATE ROOT 2* (*LPR2*), which encodes a ferroxidase. Since the biological processes of roots might be artificially affected by photo-Fenton reactions resulting from the light-irradiated rooting conditions^{20,21}, a shaded rooting system was used in our study. We further identified a mechanism that connects remodeling of root development to NH_4^+ stress: the NH_4^+ induces massive Fe

accumulation in phloem via the action of LPR2, and as a result, arrests PR development due to the inhibition of phloem function.

Results

The NH_4^+ -sensitive phenotype of PRs depends on the action of LPR2. An NH_4^+ -insensitive Arabidopsis mutant *isas* was initially screened from a T-DNA insertion library²² using transparent Petri dishes with a light-irradiated rooting medium. This mutant was found to be the SALK_056696 line, with the T-DNA insertion in the second exon of *LPR2* (AT1G71040) (Supplementary Fig. 1a, b). qRT-PCR and immunoblot assay showed that *isas* is most probably a *LPR2* knockout mutant (Supplementary Fig. 1c, d). As natural soils normally have pH-buffering capacity, the pH buffer MES was added to the growth media in our study, unless specified otherwise. When grown on a control medium with NO_3^- as the N source, the *isas* roots did not differ morphologically from wild-type Col-0 roots. In the medium with NH_4^+ as the N source, however, the *isas* mutants showed better PR growth than Col-0 seedlings did (Supplementary Fig. 2).

Unless specified otherwise, we used a black plastic sheet to cover the roots to exclude light irradiation in the remaining studies (Supplementary Fig. 3). Under such root-shaded conditions, the *isas* mutants still had greater PR elongation in the NH_4^+ -N source than Col-0 seedlings did (Fig. 1a, b). In addition, another T-DNA insertion mutant, *lpr2-1* (SALK_091930)²³, which is also probably a knockout mutant (Supplementary Fig. 1), had a similar NH_4^+ -insensitive phenotype. The NH_4^+ sensitivities of both *lpr2* mutants were also examined in unbuffered conditions, and both mutants consistently had better PR growth than Col-0 seedlings did in the NH_4^+ -N source without MES (Supplementary Fig. 4). These results show that the inhibitory effect of NH_4^+ on PR growth could be uncoupled by disruption of LPR2.

LPR1 (AT1G23010) is a close paralog of LPR2²³. However, the NH_4^+ -sensitive PR phenotype of the *lpr1-1* mutant did not differ from that of Col-0 seedlings (Fig. 1a, b). Moreover, the *lpr1lpr2* double mutants did not have greater insensitivity to NH_4^+ than *lpr2* single mutants did. Accordingly, the NH_4^+ sensitivity of PRs was only associated with LPR2 and not with LPR1. We also generated *pLPR2::LPR2-YFP* transformants in the *lpr2-1* background. These complementation lines (COM#7 and COM#15) had moderately higher LPR2 expression and LPR2 abundance than Col-0 seedlings did (Supplementary Fig. 5) and fully restored the inhibitory effect of NH_4^+ on PR growth (Fig. 1c). These results further demonstrate that LPR2 is responsible for the NH_4^+ sensitivity of PRs.

Root elongation is controlled by cell division and differentiation along the longitudinal axis of the root²⁴. Here, we showed that the meristematic cell numbers in PRs of Col-0 and COM#7 seedlings in the NH_4^+ -N source were both decreased by ~60% compared with those in the NO_3^- -N source, whereas only a slight decrease was observed in *lpr2-1* mutants (Fig. 1d). This indicates that LPR2 acts to accelerate a shift from cell division to differentiation. In addition, both the elongation cell number and the first differentiated cell length in PRs of Col-0 and COM#7 seedlings were also greatly reduced by NH_4^+ , and such reductions were clearly diminished in the *lpr2-1* PRs (Fig. 1e, f). As a result, in the NH_4^+ , the *lpr2-1* mutants had less growth stunting in the root growth zone (meristem plus elongation zone) than Col-0 and COM#7 seedlings did (Fig. 1g). Therefore, the PR growth inhibition resulting from NH_4^+ stress highly depends on LPR2 and is initiated by an accelerated shift from cell division to differentiation in the meristem zone, followed by early differentiation of elongating cells.

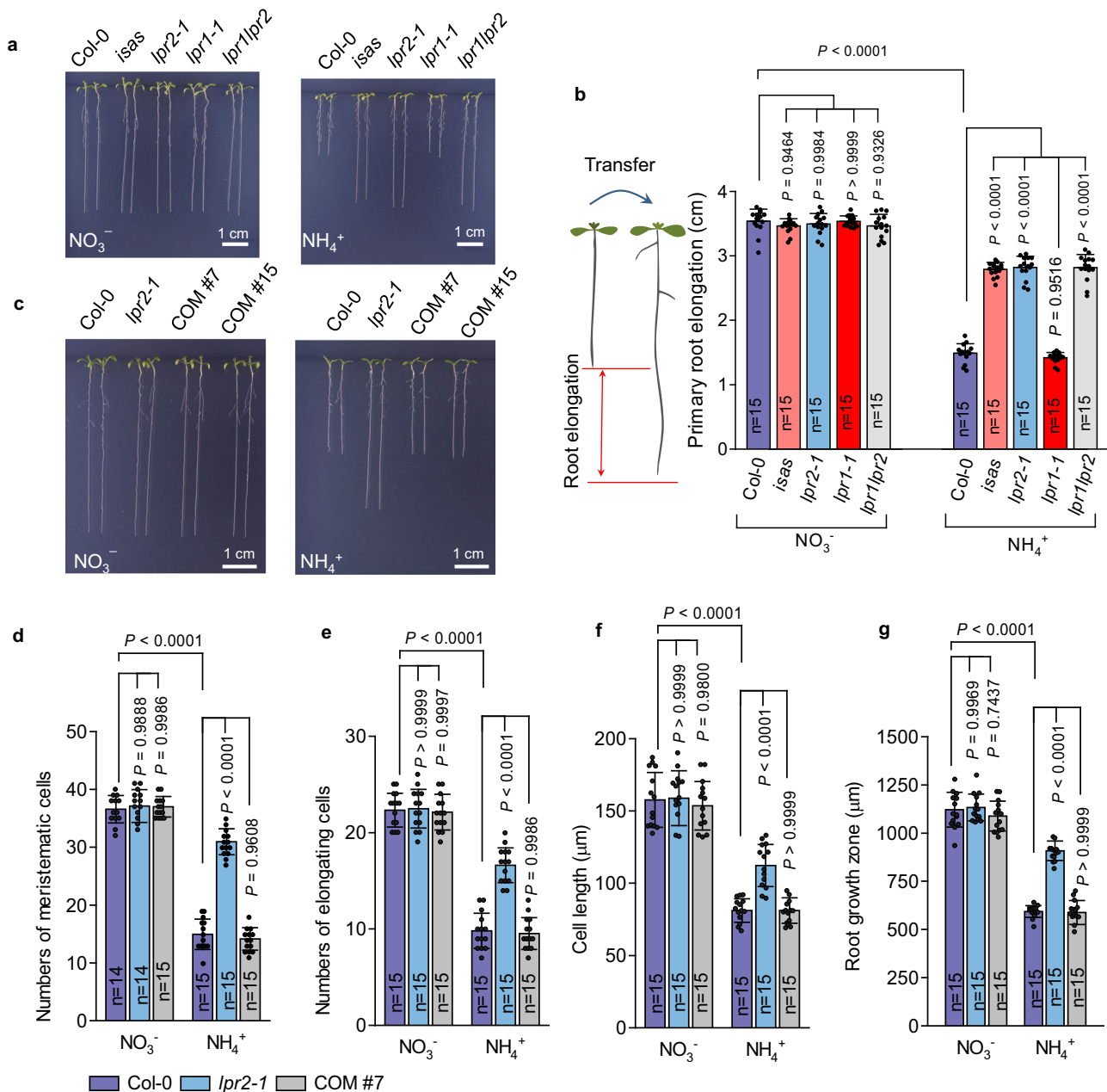


Fig. 1 LPR2-dependent growth inhibition of primary roots in NH_4^+ medium. **a** Phenotype comparison of Col-0 and the *isas*, *lpr2-1*, *lpr1-1*, and *lpr1lpr2* mutants. **b** Elongation of primary roots. **c** Phenotype comparison of Col-0, *lpr2-1*, and complementation lines (COM #7 and COM #15). **d** Number of meristematic cells. **e** Number of elongating cells. **f** Length of the first differentiated cell. **g** Length of the root growth zone (elongation plus meristem zone). **b**, **d**–**g** Data shown are mean \pm SD. *P* values < 0.05 indicate significant differences (two-way ANOVA with post-hoc Tukey HSD test; *n* = number of seedlings). Four-day-old seedlings of the indicated genotypes were transferred to NO_3^- or NH_4^+ medium with 100 μM Fe and analyzed 4 days after seedling transfer. Each experiment was repeated independently at least three times with similar results, and a representative experiment is shown.

LPR2 encodes a cell wall ferroxidase and is irreplaceable by LPR1. Prediction by the SignalP 5.0 algorithm²⁵ showed that both LPR1 and LPR2 contained a putative secretory signal peptide at the N-terminal region (Supplementary Fig. 6). Consistent with this prediction, confocal analysis of *p35S::LPR2-GFP* transformants revealed that LPR2-GFP fluorescence mainly resided in the cell wall matrix (Fig. 2a, b), which is very similar to the subcellular localization of LPR1²⁶. LPR1 was previously characterized to have ferroxidase activity that converts Fe^{2+} to Fe^{3+} .^{26,27} As expected, the recombinant GST-LPR2 protein from *Escherichia coli* also had obvious ferroxidase activity, and exhibited a typical

Michaelis–Menten kinetic with a K_m and V_{max} of 17.43 μM and 22.10 $\mu\text{M}/\text{min}/\text{mg}$ protein, respectively (Fig. 2c, d).

Considering the similarities of LPR2 and LPR1 in both subcellular localization and enzymatic reaction, we explored whether the role of LPR2 in mediating NH_4^+ sensitivity could be filled by LPR1. We used the *LPR2* promoter to confine the site of *LPR1* expression in the *lpr2-1* mutant. However, although both *pLPR2::LPR1^{CDS}/lpr2-1* and *pLPR2::LPR1^{genomic}/lpr2-1* transformants had comparable or slightly higher expression levels of *LPR1* compared with that of *LPR2* in Col-0 seedlings (Supplementary Fig. 7), they still showed similar PR growth as that of the

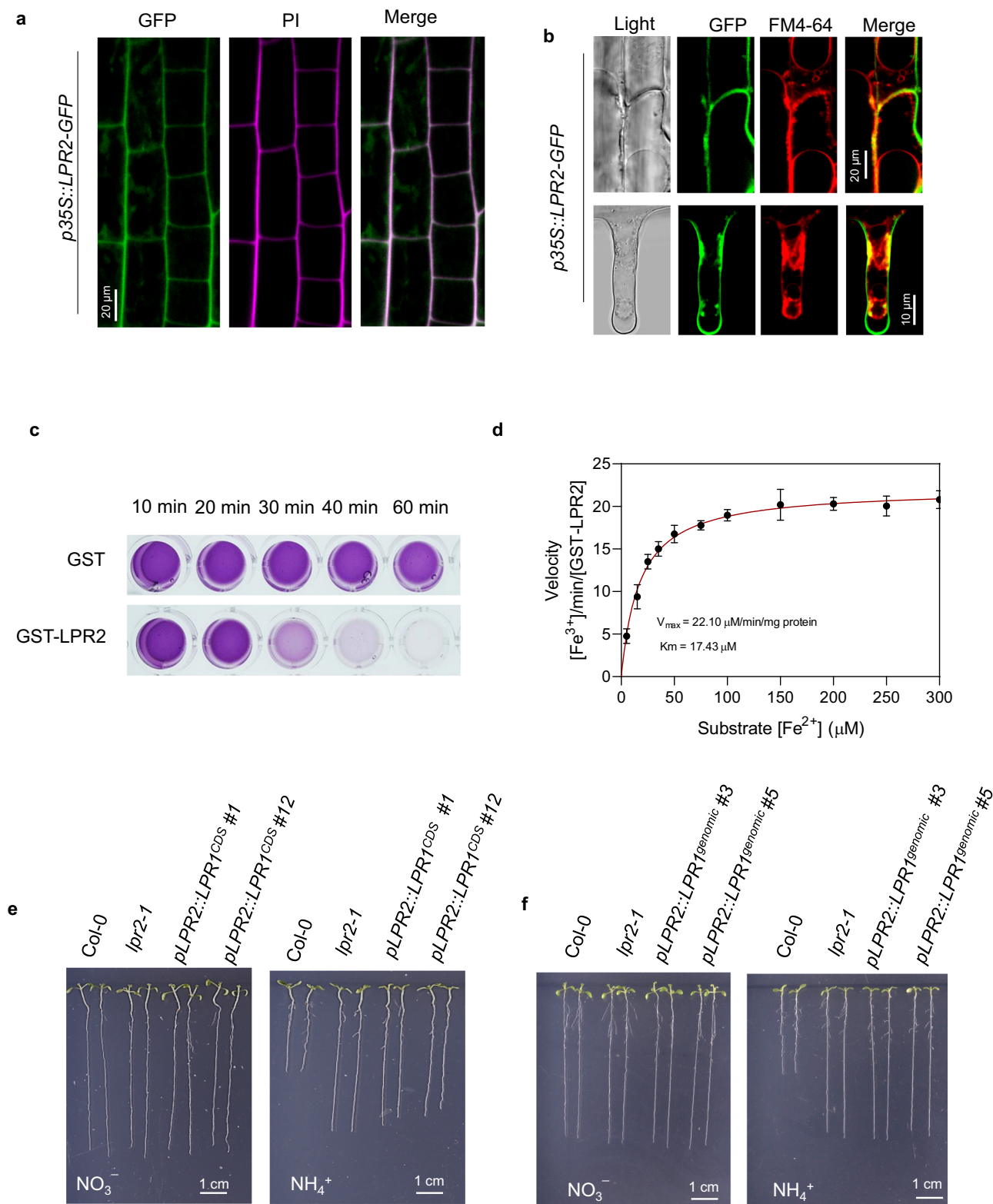


Fig. 2 LPR2 is a cell wall ferroxidase and is irreplaceable by LPR1. **a** Fluorescence co-localization of LPR2-GFP and propidium iodide in cells of *p35S::LPR2-GFP* roots. **b** Fluorescence of LPR2-GFP and FM4-64 in cells of *p35S::LPR2-GFP* roots after plasmolysis with 0.8 M sorbitol. Four-day-old seedlings were transferred to NH_4^+ medium with 100 μM Fe, and confocal analyses were performed 4 days after seedling transfer. **c** Ferroxidase activities of recombinant GST-LPR2. Ferroxidase assay using 1 μg purified GST-LPR2 protein. Pink indicates the Fe^{2+} -ferrozine complex. The substrate Fe^{2+} was added in the form of $\text{Fe}(\text{NH}_4)_2(\text{SO}_4)_2 \cdot 6\text{H}_2\text{O}$ at an initial concentration of 50 μM . **d** Fe^{2+} concentration-dependent (0–300 μM) ferroxidase activity of GST-LPR2 protein. Data shown are mean \pm SD of three biological replicates. **e, f** Phenotype of *lpr2-1* mutant lines with LPR2 promoter-confined tissue-specific expression of *LPR1^{CDS}* and *LPR1^{genomic}*. Four-day-old seedlings of the indicated genotypes were transferred to NO_3^- or NH_4^+ medium with 100 μM Fe and analyzed 4 days after seedling transfer. Two (**c, d**) or three (**a, b, e, f**) independent experiments were performed with similar results, and one representative experiment is shown.

lpr2-1 seedlings in the NH_4^+ -N source (Fig. 2e, f). Therefore, LPR2 is irreplaceable by LPR1 in mediating NH_4^+ sensitivity, which may explain why only LPR2 and not LPR1 acts to suppress PR growth in the presence of NH_4^+ .

The LPR2-mediated NH_4^+ -sensitive PR phenotype depends on the action of Fe. We next asked how LPR2 mediates the NH_4^+ sensitivity of PRs. Disruption of LPR2 did not affect the NH_4^+ level in roots (Supplementary Fig. 8), showing that LPR2-mediated NH_4^+ sensitivity is not associated with NH_4^+ accumulation. Since LPR2 is a ferroxidase, the role of Fe in regulating NH_4^+ sensitivity of PRs was investigated. We first grew Arabidopsis seedlings in media with different doses of Fe. Fe doses $\leq 10 \mu\text{M}$ ensured a similar PR growth of Col-0 between NH_4^+ - and NO_3^- -N sources, whereas $\geq 50 \mu\text{M}$ induced a clear dose-dependent inhibition of PR growth in the NH_4^+ -N source (Supplementary Fig. 9 and Fig. 3a). In contrast, supplementing deferoxamine or ferrozine, two potent Fe chelators, almost completely rescued PR growth of Col-0 seedlings in the NH_4^+ -N source with $100 \mu\text{M}$ Fe (Supplementary Fig. 10). The inhibitory effect of NH_4^+ on root growth of rice plants was also uncoupled by lowering Fe supply (Supplementary Fig. 11). These results indicate that the NH_4^+ sensitivity of roots strongly depends on the action of Fe.

Given that Fe-free ($0 \mu\text{M}$) and high-Fe ($\geq 200 \mu\text{M}$) conditions may respectively cause Fe deficiency and Fe excess in Arabidopsis, we used 10 and $100 \mu\text{M}$ Fe, defined as low Fe (Fe^{low}) and sufficient Fe (Fe^{suff}), respectively, in the remaining evaluations. The difference in NH_4^+ sensitivity between *lpr2* mutants and either Col-0 or COM#7 seedlings was completely abolished when the Fe concentration was lowered from Fe^{suff} to Fe^{low} (Fig. 3b), showing that the LPR2-mediated NH_4^+ -sensitive phenotype depends on the action of Fe.

Furthermore, we tested whether Fe plays a role in NH_4^+ sensitivity of PRs when the N source has a high $\text{NH}_4^+/\text{NO}_3^-$ ratio (10:2). Similarly, the difference in PR growth inhibition between *lpr2* mutants and Col-0 seedlings at a high $\text{NH}_4^+/\text{NO}_3^-$ ratio was also abolished by lowering Fe supplement (Supplementary Fig. 12). Therefore, Fe is required for the remodeling of PR development when NH_4^+ is the only or predominant N source.

NH_4^+ induces Fe deposition in the phloem. The strong dependence of the NH_4^+ -sensitive PR phenotype on Fe raised the question of whether NH_4^+ stress affects Fe deposition in roots. We used an Fe-specific histochemical procedure, Perls/3,3'-diaminobenzidine (DAB) staining²⁸, to visualize Fe distribution in PRs. For Col-0 and *lpr1-1* seedlings with Fe^{suff} , the NH_4^+ -N source resulted in massive Fe deposition in root stele compared to that of the NO_3^- -N source (Fig. 3c and Supplementary Fig. 13a). In contrast, the NH_4^+ -induced Fe deposition was completely abolished by either disruption of LPR2 in *lpr2-1* mutants or Fe^{low} treatment in Col-0 seedlings. The complementation line COM#7 restored the Fe deposition in root stele in the NH_4^+ -N source with Fe^{suff} . These results indicate that NH_4^+ -induced Fe deposition in root stele depends on LPR2 as well as on a sufficient Fe supply. Notably, these respective Fe depositions across the various genotypes and Fe-dose treatments were negatively correlated with PR growth in the NH_4^+ -N source (Fig. 3b), suggesting that the Fe deposition in root stele determines the PR growth response to NH_4^+ stress. Surprisingly, in the presence of either NO_3^- or NH_4^+ , Fe^{low} treatment resulted in a higher Fe deposition in the root stem cell niche (SCN) of Col-0, *lpr2-1*, and COM#7 seedlings compared with that with Fe^{suff} treatment (Fig. 3c). Nevertheless, although no Fe deposition was detected in the SCN of *lpr1lpr2* seedlings (Supplementary Fig. 13b), this

double mutant displayed similar NH_4^+ insensitivity as that of the *lpr2-1* mutant (Fig. 1c), indicating that the NH_4^+ sensitivity of PRs is independent of the Fe deposition in SCN.

A close-up view of Perls/DAB-stained Col-0 roots from Fe^{suff} NH_4^+ treatment showed that the greatest Fe deposition was in phloem cells (Fig. 3d). At higher magnification, Fe was found to be mainly located at the periphery of sieve elements (Fig. 3e). This periphery is probably the apoplast of phloem, because the LPR2 responsible for this Fe deposition is a cell wall-resident protein. Since the phloem vasculature was difficult to plasmolyze using the methods of osmotic dehydration, we used acetone to wash off the plasmalemma. This procedure did not alter Fe deposition at the periphery of sieve elements (Fig. 3f), providing further support for apoplastic Fe deposition in the phloem.

Unexpectedly, the NH_4^+ -N source with Fe^{suff} resulted in heavy Fe deposition in all cell types of Col-0 PRs under light-irradiated rooting conditions, which was significantly different from that observed under root-shaded conditions (Supplementary Fig. 14). The result strongly suggests that the impact of artificial light irradiation on roots cannot be neglected in studying the mechanisms of root growth responses to NH_4^+ , even though root growth inhibition by NH_4^+ is barely affected by the light irradiation on roots.

LPR2 distributes in root stele and is upregulated by NH_4^+ . The NH_4^+ -induced phloem-specific Fe deposition prompted us to analyze the tissue distribution of LPR2 in PRs of *pLPR2::LPR2-YFP/lpr2-1* transformants. LPR2-YFP was mainly distributed in the root stele, but its abundance was lower in the NO_3^- -N source. LPR2-YFP fluorescence was increased in the NH_4^+ -N source, while the dose of Fe had little effect on this response (Fig. 4a). Unexpectedly, LPR2 was found to be ubiquitously distributed in the whole root stele except in the xylem (Fig. 4b), an area much larger than the Fe deposition region (i.e., phloem). This suggests that other factor(s) are required for phloem-specific Fe deposition and NH_4^+ -induced PR growth inhibition. Unfortunately, we were unable to identify the relative factor(s) in the present study.

LPR1 distribution in PRs was also examined in *pLPR1::LPR1-YFP/lpr1-1* transformants. The abundance of LPR1-YFP was lower in the presence of either N source, but it was mainly distributed in the SCN of the root apical meristem and slightly expanded to endodermal cell layers (Supplementary Fig. 15). The difference in tissue distribution may be another part of the explanation of why LPR1 does not play a role in mediating the NH_4^+ -sensitive phenotype as LPR2 does.

The response of LPR2 in Col-0 roots to NH_4^+ was also examined. Consistent with the above confocal result, either the LPR2 expression or the LPR2 abundance in Col-0 roots showed an increase under NH_4^+ relative to that under NO_3^- , which was also irrespective of the Fe supplementation dose (Fig. 4c–e). Therefore, NH_4^+ rather than Fe upregulates LPR2. Interestingly, although the LPR2 expression in *p35S::LPR2-GFP* overexpression lines was similar between two N sources, the LPR2-GFP abundance in the NH_4^+ -N source was higher than that in the NO_3^- -N source (Supplementary Fig. 16), indicating a post-transcriptional regulation for LPR2. It is worth noting that, although LPR2 was slightly overexpressed in *pLPR2::LPR2-YFP/lpr2-1* complementation lines (Supplementary Fig. 5), their PRs had a similar NH_4^+ -sensitive phenotype as that of Col-0 seedlings (Fig. 1d). Furthermore, the PRs of *p35S::LPR2-GFP* overexpression lines also had a similar NH_4^+ sensitivity as that of Col-0 PRs (Supplementary Fig. 17a). These results indicate that the upregulated portion of LPR2 makes little contribution to NH_4^+ sensitivity and further support that, although LPR2 is essential, additional factor(s) are also required for NH_4^+ -induced PR

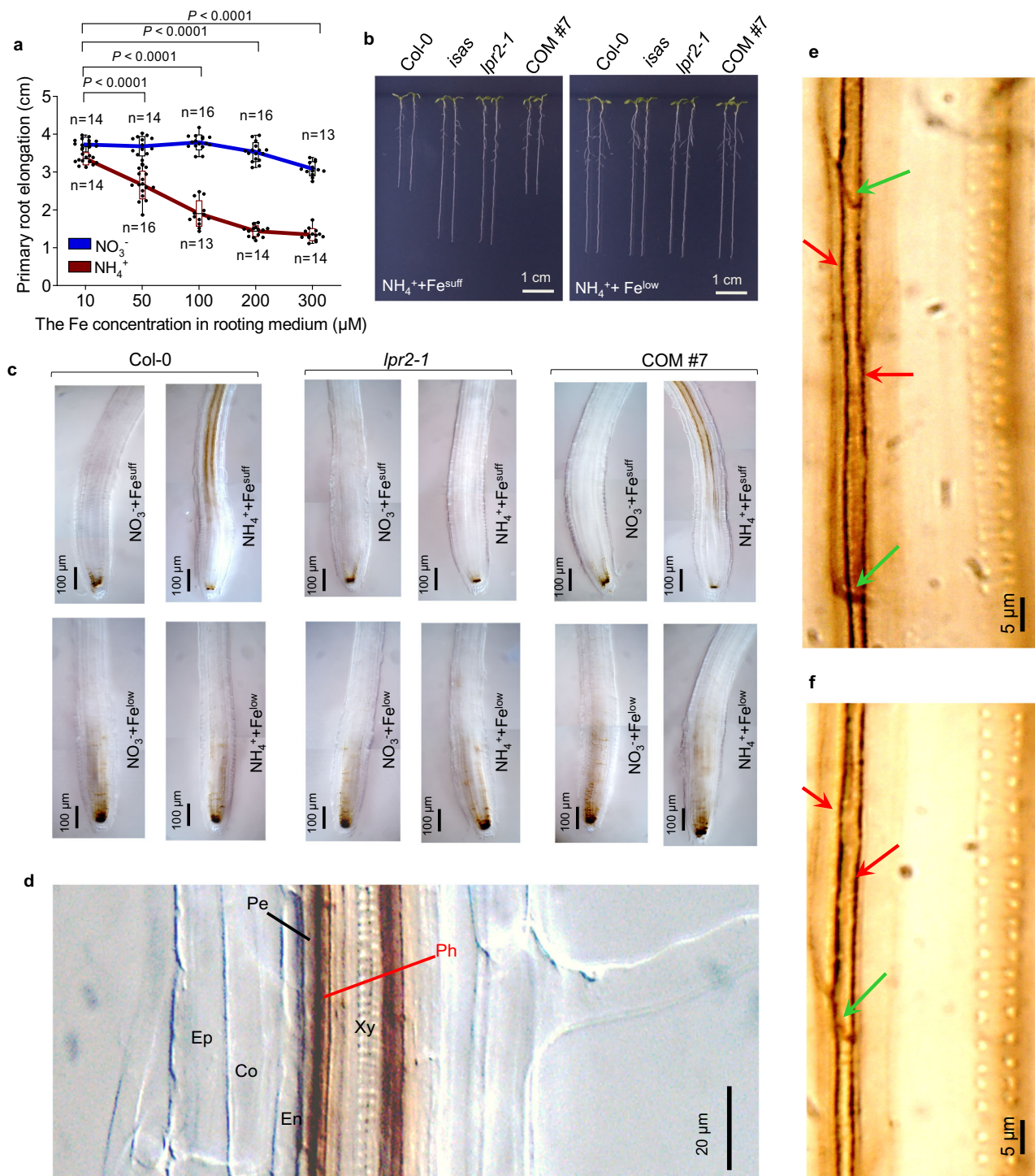


Fig. 3 Fe-dependent inhibition of primary root growth in NH₄⁺ medium. **a** Primary root elongation of Col-0 seedlings in NO₃⁻-N or NH₄⁺-N source with various doses of Fe. Center line represents mean and bounds of box are SD; whiskers indicate the minimum and maximum values; *n* = number of seedlings. *P* values <0.05 indicate significant interactions between N form and Fe dose (two-way ANOVA with post-hoc Tukey HSD test). **b** NH₄⁺-sensitivity comparison of Col-0, *isas*, *lpr2-1*, and complementation line COM #7 in Fe^{suff} (100 µM) and Fe^{low} (10 µM) conditions. **c** Fe deposition indicated by Perls/DAB staining in primary roots. **d** Close-up view of Fe deposition in root stele of Col-0 seedlings grown in Fe^{suff} NH₄⁺ medium. Ep epidermis, Co cortex, En endodermis, Pe pericycle, Ph phloem, Xy xylem. **e** Perls/DAB staining in the phloem of the primary roots of Col-0 seedlings grown in Fe^{suff} NH₄⁺ medium. Red and green arrows show Fe depositions at lateral cell walls and sieve plates of the phloem, respectively. **f** Acetone washed-Perls/DAB staining in phloem of the primary roots of Col-0 seedlings grown in Fe^{suff} NH₄⁺ medium. The Perls/DAB-stained roots were washed with acetone for 3 h. Four-day-old seedlings of the indicated genotypes were transferred to NO₃⁻ or NH₄⁺ medium with various doses of Fe supply and analyzed 4 days after seedling transfer. Each experiment was repeated independently three times with similar results, and a representative experiment is shown.

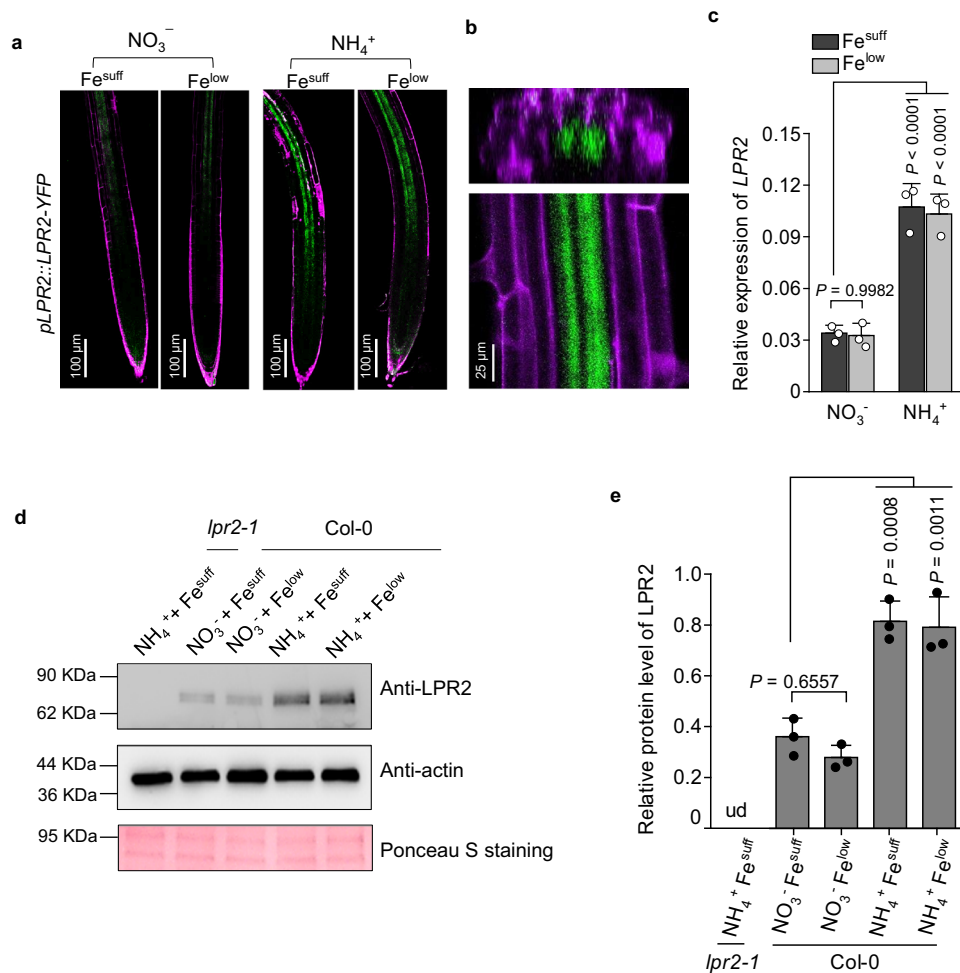


Fig. 4 Distribution of LPR2 in roots and its response to NH_4^+ . **a** $pLPR2::LPR2-YFP$ expression in primary roots of complementation line COM#7. Roots were counterstained with propidium iodide (purple fluorescence) and analyzed for YFP fluorescence (green). **b** Radial section (top) and close-up view (bottom) of $pLPR2::LPR2-YFP$ expression in a root of a COM#7 seedling grown in Fe^{suff} NH_4^+ medium. **c** LPR2 expression in Col-0 roots. Relative expression levels were normalized to the geometric mean of expression of *UBQ10* and *Ef1 α* . **d**, **e** Representative gels and relative protein levels in Col-0 roots. Relative LPR2 levels were estimated from the ratio of the signal intensity of LPR2 to that of actin from the same sample. **c**, **e** Data shown are mean \pm SD of three biological replicates. *P* values < 0.05 indicate significant differences (two-way ANOVA with post-hoc Tukey HSD test). Four-day-old seedlings of the indicated genotypes were transferred to NO_3^- or NH_4^+ medium with Fe^{suff} (100 μM) or Fe^{low} (10 μM) and analyzed 4 days after seedling transfer. Each experiment was repeated independently three times with similar results, and a representative experiment is shown.

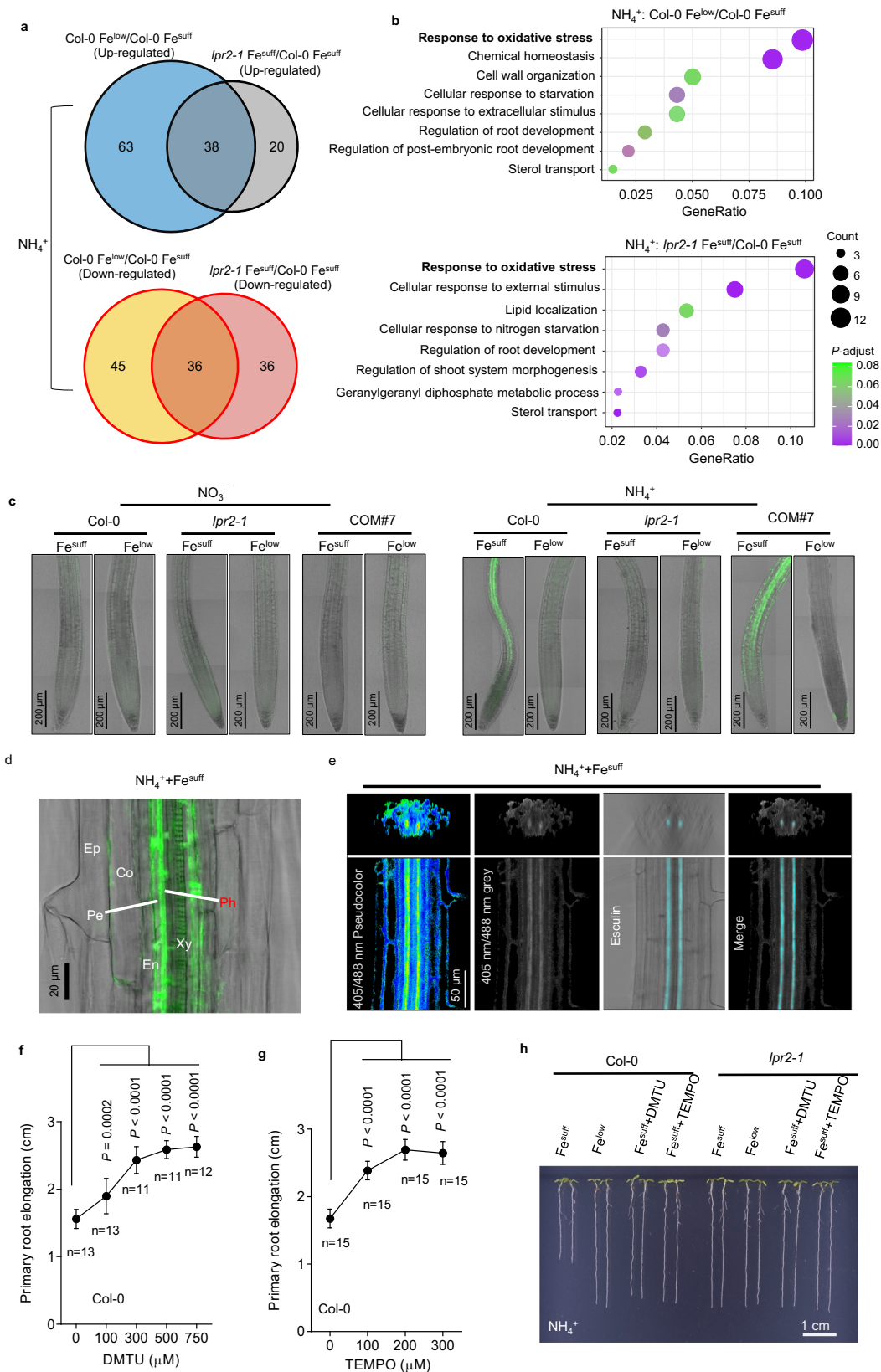
growth inhibition. It is worth noting that the *p35S::LPR2-GFP* overexpression lines showed irregular Fe deposition in PRs in the NH_4^+ -N source (Supplementary Fig. 17b), indicating that NH_4^+ -induced phloem-specific Fe deposition depends on the stele-specific distribution of LPR2.

NH_4^+ -induced Fe deposition triggers a burst of reactive oxygen species (ROS). To understand how LPR2-mediated Fe deposition inhibits PR growth in the NH_4^+ -N source, we performed a whole transcriptome sequencing (RNA-seq) analysis of gene expression in the roots of Col-0 and *lpr2-1* seedlings (Supplementary Data 1a). The reliability of RNA-seq data was confirmed by qRT-PCR assay for the expression of ten randomly selected genes with different abundances (Supplementary Fig. 18). As Fe^{low} treatment and LPR2 disruption similarly alleviated PR growth inhibition in the NH_4^+ -N source, we screened differentially expressed genes (DEGs) ($-1 > \log_2[\text{fold change}] > 1$; *P* value < 0.05) by performing pairwise comparisons of transcript abundances either between the two Fe treatments or between *lpr2-1* and Col-0 with Fe^{suff} treatment (Supplementary Data 1b–e). In the NO_3^- -N source, there were only 11 DEGs between the two Fe

treatments for Col-0 seedlings and 87 DEGs between the two genotypes that received Fe^{suff} treatment (Supplementary Fig. 19a, b). These DEGs are unlikely related to PR development because either Fe^{low} treatment or LPR2 disruption had little effect on PR growth in NO_3^- -N source.

We subsequently focused on DEGs in the NH_4^+ -N source. There were 182 DEGs (101 upregulated; 81 downregulated) between two Fe treatments for Col-0 seedlings and 130 DEGs (58 upregulated; 72 downregulated) between two genotypes that received Fe^{suff} treatment (Fig. 5a and Supplementary Fig. 19c, d). In these two comparisons, however, we did not find any DEGs currently known to be related to NH_4^+ toxicity (Supplementary Data 1f). Interestingly, the ratio of overlapped DEGs in the above two comparisons was high (Fig. 5a), and Gene Ontology (GO) enrichment analysis showed that the biggest cluster in both comparisons was related to “response to oxidative stress” (Fig. 5b).

The above results prompted us to monitor ROS formation in roots. We first histologically visualized ROS using 2',7'-dichlorodihydrofluorescein diacetate (H_2DCFDA), a fluorescent ROS indicator. The data showed that NH_4^+ resulted in clear



ROS formation in root stele, which depended on either LPR2 action or sufficient Fe supplementation (Fig. 5c). The ratio-metric fluorescent reporter protein roGFP2-Orp1 was recently shown to report the level of intracellular H₂O₂²⁹. Because of the passage of extracellular H₂O₂ across the plasma membrane via aquaporins^{30,31}, the extracellular H₂O₂ formation can also be

indirectly reflected by roGFP2-Orp1 reporter in its neighboring cells²⁹. Consistent with the observed ROS formation, the roGFP2-Orp1 reporter showed that NH₄⁺ also triggered a burst of H₂O₂ in root stele under Fe^{suff} conditions (Supplementary Fig. 20). A close-up view of H₂DCFDA-stained roots revealed that the NH₄⁺-triggered burst of ROS mainly occurred in the

Fig. 5 Fe-dependent primary root growth inhibition by NH_4^+ is associated with a burst in reactive oxygen species (ROS). **a, b** Venn diagram and Gene Ontology enrichment analysis of differentially expressed genes (DEGs) that are up- and downregulated in the pairwise comparisons of Col-0 Fe^{low} vs. Col-0 Fe^{suff} and *lpr2-1* Fe^{suff} vs. Col-0 Fe^{suff} in the NH_4^+ -N source. The size of the circle represents gene numbers, and the color represents the value of P -adjust the was calculated by hypergeometric tests and adjusted for multiple testing using FDR. RNA sequencing was conducted with three biological replicates per line and condition. **c** ROS visualization in primary roots of Col-0, *lpr2-1*, and complementation line COM#7 seedlings by H_2DCFDA staining. **d** Close-up view of H_2DCFDA staining in primary roots of Col-0 seedlings grown in Fe^{suff} NH_4^+ medium. **e** Co-localization of false color representation of H_2O_2 and fluorescence of phloem marker esculin in primary roots of roGFP2-Orp1 seedlings grown in Fe^{suff} NH_4^+ medium. **f, g** Dose-response relationship of the primary root elongation of Col-0 seedlings plotted as a function of the concentration of ROS scavengers. Data shown are mean \pm SD. n = number of seedlings. P values < 0.05 indicate significant differences (one-way ANOVA with post-hoc Tukey HSD test). **h** Images of the effects of 750 μM dimethyl thiourea (DMTU) and 200 μM 4-hydroxy-TEMPO (TEMPO) on Col-0 seedlings. Four-day-old seedlings of the indicated genotypes were transferred to NO_3^- or NH_4^+ medium with Fe^{suff} (100 μM) or Fe^{low} (10 μM) with or without the indicated ROS scavengers. Analyses were performed 4 days after seedling transfer. The experiments (**c-h**) were repeated independently three times with similar results, and representative data from one experiment are shown.

phloem (Fig. 5d) and resembled the pattern of NH_4^+ -induced Fe deposition. This finding was further supported by the roGFP2-Orp1 reporter in that the NH_4^+ -induced H_2O_2 accumulation was overlaid well with the phloem marker esculin (Fig. 5e).

ROS act downstream of Fe deposition to mediate growth response to NH_4^+ . The above results implied that the remodeling of root development in response to NH_4^+ stress may be associated with a burst of ROS. Therefore, ROS scavengers were used to test this assumption. Unexpectedly, the addition of either ascorbic acid (ASA) or glutathione (GSH) to the NH_4^+ medium with Fe^{suff} resulted in greater inhibition of PR growth. This is probably because either ASA or GSH can enhance the production of hydroxyl radicals ($\cdot\text{OH}$)—one of the most deleterious ROS—under Fe-rich conditions by Fenton reactions³². We also tested the effect of the H_2O_2 scavenger potassium iodide, but this compound showed high toxicity to plants in our growth condition because it could inhibit PR growth even in the NO_3^- medium. Thus, we used other milder ROS scavengers, including dimethyl thiourea (DMTU) and 4-hydroxy-TEMPO (TEMPO), to counteract excess ROS production. Application of either of these scavengers to Col-0 seedlings had little effect on the growth of PRs in NO_3^- medium with Fe^{suff} (Supplementary Fig. 21) but significantly restored PR growth in NH_4^+ medium with Fe^{suff} in a dose-dependent manner (Fig. 5f–h). The result suggests that Fe-dependent PR growth inhibition in NH_4^+ -N source could be associated with excessive ROS formation.

We also examined Fe deposition after DMTU and TEMPO treatments. Although the PR growth of Col-0 seedlings in Fe^{suff} NH_4^+ medium was restored in the presence of ROS scavengers, Fe deposition in root phloem was still observed (Supplementary Fig. 22). Therefore, ROS very likely act downstream of Fe deposition to remodel root development in the NH_4^+ -N source. However, application of either ROS scavenger lengthened the distance between the starting site of NH_4^+ -induced Fe deposition and the root tip. This is probably associated with improved development of the root growth zone owing to ROS scavengers.

NH_4^+ induces callose deposition in the phloem. There is growing evidence that ROS regulates callose deposition³³. We, therefore, examined callose formation by aniline blue staining (Fig. 6a). For Fe^{suff} -treated Col-0 seedlings, the NH_4^+ -N source resulted in massive callose deposition in root stele relative to that with the NO_3^- -N source. This NH_4^+ -induced callose deposition was completely inhibited by either disruption of LPR2 in *lpr2-1* seedlings or Fe^{low} treatment in Col-0 seedlings. The complementation line COM#7 behaved similarly to Col-0. Therefore, NH_4^+ induces callose deposition in root stele in LPR2- and Fe-dependent manners. Furthermore, both the close-up and the

radial section views of the Fe^{suff} NH_4^+ Col-0 roots showed that callose deposition was mainly localized in two poles of the root stele (Fig. 6b).

To determine the cell type for these two poles, aniline blue staining was performed in roots of *pSUC2::GFP-sporamin* transformants in which the GFP-sporamin marker was restricted in the phloem files, including sieve elements and companion cells³⁴. Confocal analysis revealed that the aniline blue staining overlaid well with the GFP-sporamin marker in the roots subjected to Fe^{suff} NH_4^+ treatment, showing that NH_4^+ -dependent callose deposition is localized in the phloem (Fig. 6c). At high magnification, callose was found to be located at the periphery of sieve elements (Supplementary Fig. 23), which is strikingly similar to the localization of the Fe deposition.

It is worth noting that, although neither DMTU nor TEMPO abolished the NH_4^+ -induced Fe deposition in the root phloem (Supplementary Fig. 22), they substantially blocked callose deposition in the phloem (Fig. 6d). Therefore, the burst of ROS acts downstream of Fe deposition to induce callose deposition in response to NH_4^+ stress.

Impaired phloem action is responsible for the growth response to NH_4^+ . As callose deposition in the phloem may affect phloem action, the phloem-mobile probe esculin³⁵ was used to evaluate the impacts of NH_4^+ stress on phloem action. The phloem transport velocity (PTV) was determined by dividing the distance of esculin traveled between two marks by the elapsed time³⁶. The data showed that NH_4^+ significantly inhibited the PTV in PRs of Col-0 seedlings compared with the NO_3^- -N source under Fe^{suff} conditions, whereas either disruption of LPR2 in *lpr2-1* mutants or Fe^{low} treatment in Col-0 seedlings completely reversed this inhibition. The complementation line COM#7 behaved similarly to Col-0 (Fig. 7a). We then focused on phloem unloading. Once the esculin was imported into the root tip, individual images were recorded along with their times of acquisition³⁷. As expected, NH_4^+ strongly arrested esculin unloading from phloem in the root growth zone in LPR2- and Fe-dependent manners (Fig. 7b). These results demonstrate that NH_4^+ impairs phloem function via the actions of LPR2 and Fe.

As esculin is loaded into the phloem by the sucrose transporter SUC2^{35,38}, the impaired phloem transport and unloading of esculin reflect the inhibition of sucrose supply to the root growth zone. We, therefore, examined whether the LPR2-dependent NH_4^+ -sensitive phenotype was associated with insufficient sucrose allocation to the root growth zone. Because all the above tests were performed using seedlings fed with 1% sucrose, we first needed to clarify an artificial effect from exogenous sucrose. The *lpr2-1* mutants still exhibited better PR growth than Col-0 seedlings did in the sucrose-free NH_4^+ medium, although the difference between them was slightly diminished compared with

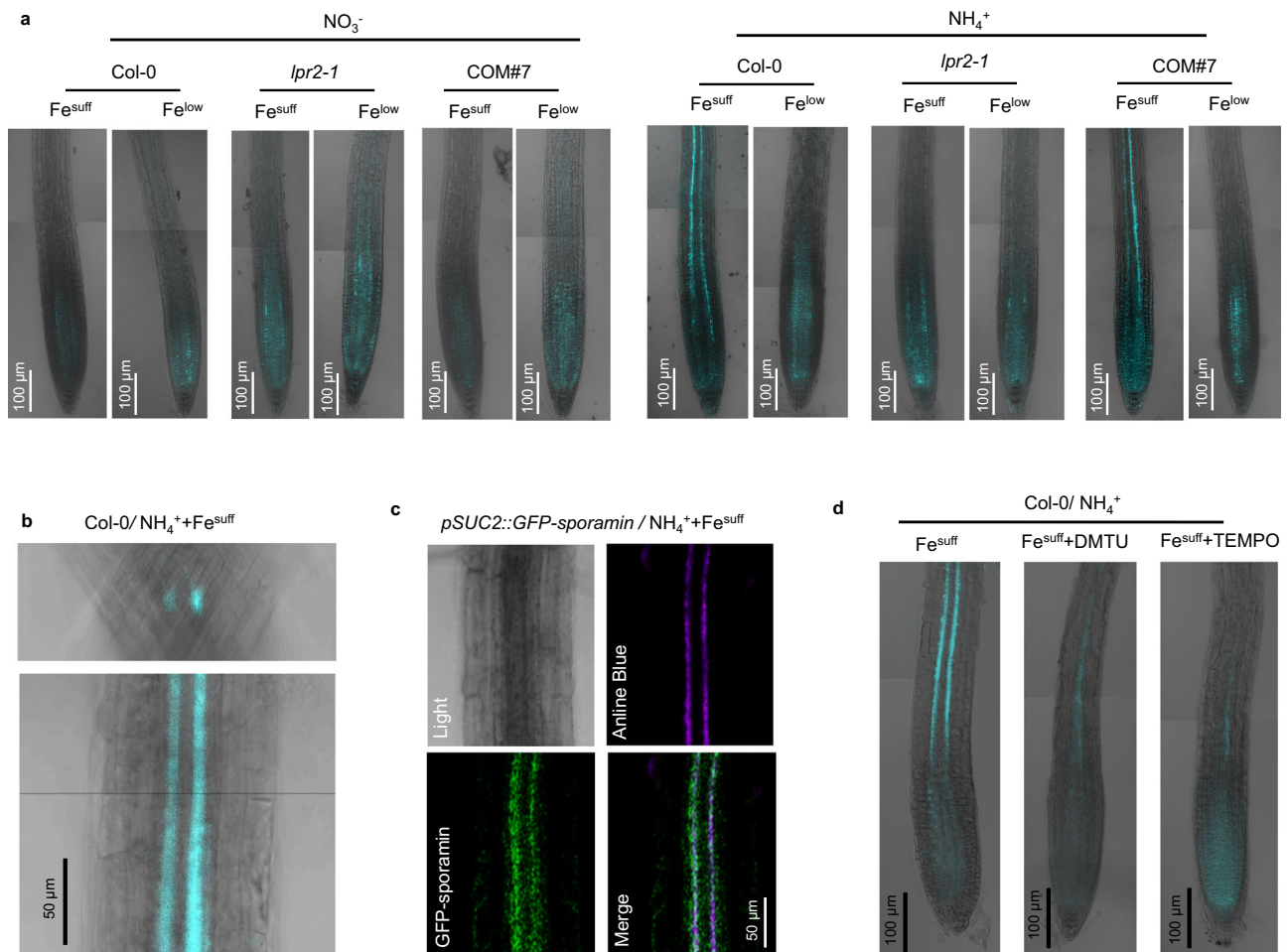


Fig. 6 Fe-dependent callose deposition in the phloem via reactive oxygen species (ROS) in response to NH_4^+ . **a** Callose detection in primary roots of Col-0, *lpr2-1*, and complementation line COM#7 seedlings by aniline blue staining. **b** Radial section (top) and close-up view (bottom) of aniline blue staining in primary roots of Col-0 seedlings grown in Fe^{suff} NH_4^+ medium. **c** Fluorescence co-localization of GFP-sporamin and aniline blue staining in *pSUC2::GFP-sporamin* roots. **d** ROS scavengers abolished the NH_4^+ -induced callose deposition. Four-day-old seedlings of the indicated genotypes were transferred to NO_3^- or NH_4^+ medium with Fe^{suff} (100 μM) or Fe^{low} (10 μM) with or without the indicated ROS scavenger. Each experiment was repeated independently three times with similar results, and a representative experiment is shown.

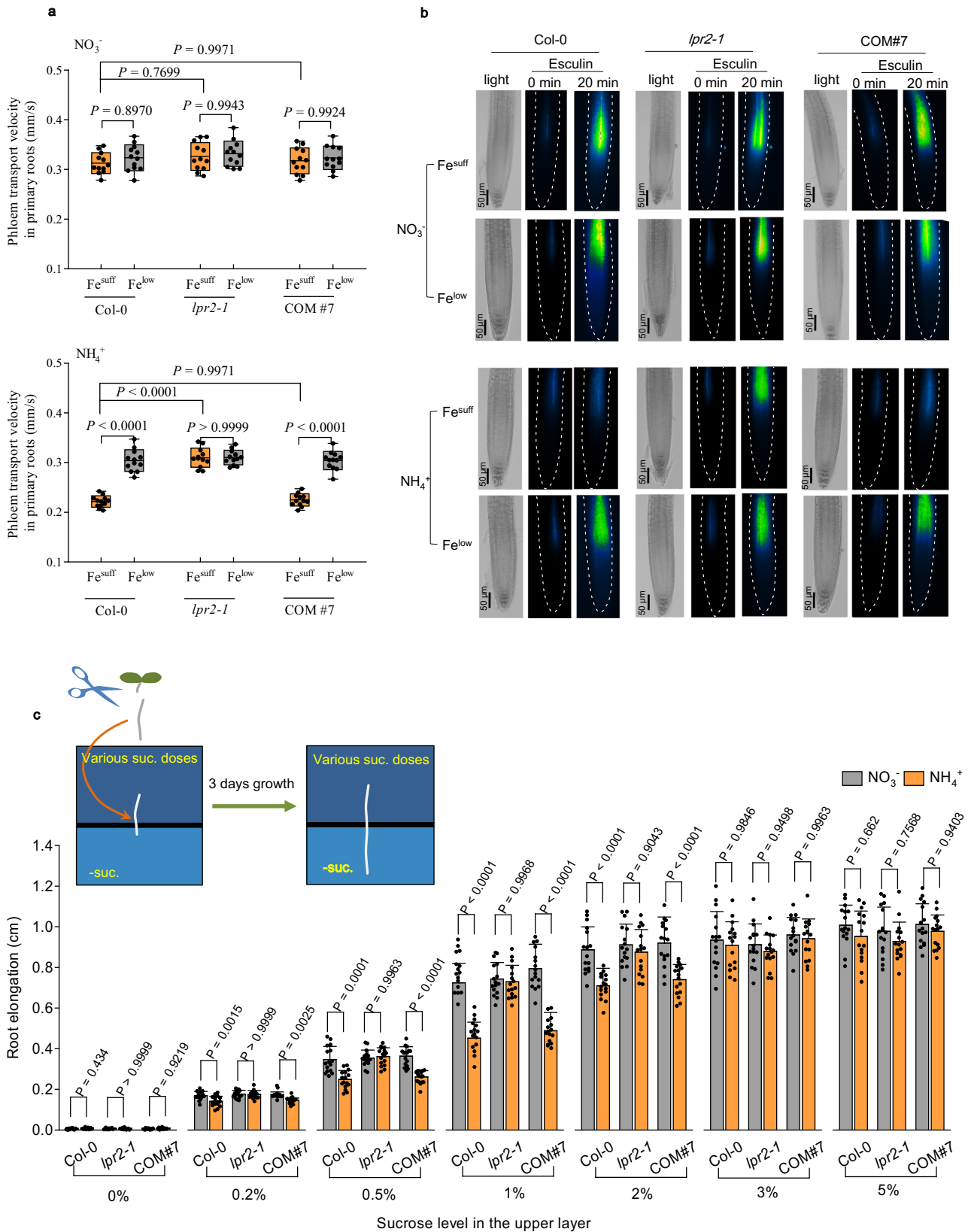
that in plants supplemented with 1% sucrose (Supplementary Fig. 24). Therefore, the genotype-specific growth response to the N source largely depends on the native biological processes of plants.

In subsequent tests, we used detached PRs to eliminate the potential effects of the sucrose source of shoots from different genotypes on their root growth. The detached PRs were transferred to a vertical two-layer split agar system with sucrose absent in the lower layer and various doses of sucrose present in the upper layer (Fig. 7c). In sucrose-free treatment, the detached PRs almost completely lost growth ability regardless of N source and genotype, indicating the importance of phloem-transported sucrose in maintaining root growth. For Col-0 seedlings, the growth difference of detached PRs between NO_3^- -N and NH_4^+ -N sources with Fe^{suff} highly depended on the dose of sucrose: the difference was the most significant with 1% sucrose treatment, but it was diminished with lower sucrose doses because PR growth was inhibited in both N sources. Notably, the inhibitory effect of NH_4^+ on the growth of detached PRs of Col-0 seedlings was completely uncoupled by the elevation of sucrose to 3% or more. The detached PRs of *lpr2-1* mutants showed similar growth between the two N sources in all sucrose treatments, probably because LPR2 disruption protected the phloem from impairment due to NH_4^+ stress. The complementation line COM#7 behaved

similarly to Col-0. Taken together, the above results point to a connection between the effect of NH_4^+ -induced stress on root morphological response and insufficient sucrose allocation resulting from inhibited phloem action.

Discussion

NH_4^+ can be directly assimilated after absorption into plant cells, whereas NO_3^- needs to be reduced to NH_4^+ in an energy-consuming manner before it can be utilized by plants^{39,40}. This raises a critically puzzling question because, although NH_4^+ is a theoretically preferred N source for plants, it inhibits PR growth when it is the only or predominant N source. Our study provides insights into the related factors that contribute to the adjustment of PR development in response to NH_4^+ stress by revealing the essential role of phloem Fe deposition in determining the NH_4^+ -sensitive phenotype of PRs. Furthermore, increased external Fe availability intensifies NH_4^+ -induced PR growth inhibition (Fig. 3a). Therefore, the occurrence of NH_4^+ toxicity in roots is not a single-factor event: Fe is also involved in this process. Notably, the conditions of soils that favor NH_4^+ formation also favor Fe solubilization. For example, in wetlands with anoxic conditions, the levels of soluble Fe can easily exceed 10 mg kg^{-1} ($\sim 180 \mu\text{mol kg}^{-1}$)^{41,42}; in acidic soils rich in NH_4^+ due to higher



ammonification than nitrification rates⁴³, the low pH also greatly increases Fe solubility⁴⁴. This close relationship between NH_4^+ and Fe in both plants and soils should be considered when developing agronomic strategies or genetically manipulated plants to cope with NH_4^+ stress.

The ferroxidase LPR2 is crucial for NH_4^+ -induced Fe deposition in the phloem (Fig. 3c). Unexpectedly, the area of LPR2 distribution in root stele is much larger than the region of phloem-specific Fe deposition. Because LPR2 mainly resides in the cell wall matrix (Fig. 2a, b), the source of LPR2 substrate from

Fig. 7 Inhibition of phloem action and sucrose complementation of primary root growth in NH_4^+ medium. **a, b** Phloem transport velocity and phloem unloading of esculin. Center line represents mean and bounds of box are SD; whiskers indicate the minimum and maximum values. P values < 0.05 indicate significant differences (two-way ANOVA with post-hoc Tukey HSD test, $n = 12$ seedlings per line and condition). Four-day-old seedlings of Col-0, *lpr2-1*, and complementation line COM#7 were transferred to NO_3^- or NH_4^+ medium with Fe^{suff} (100 μM) or Fe^{low} (10 μM) and analyzed 4 days after seedling transfer. **c** Growth response of detached primary roots to localized sucrose supply. Data shown are mean \pm SD. P values < 0.05 indicate significant differences (two-way ANOVA with post-hoc Tukey HSD test, $n = 16$ detached primary roots per line and condition). Inset: Scheme depicting the growth response analyses of detached primary roots to localized sucrose supply. Roots (1 cm) were cut from four-day-old seedlings. The detached roots were then transferred to a vertical two-layer split agar system of either NO_3^- or NH_4^+ medium with Fe^{suff} or Fe^{low} . The upper layers were treated with various doses of sucrose, and the lower layers were absent of sucrose. Analyses were performed 3 days after seedling transfer. Each experiment was repeated independently three times similar results, and a representative experiment is shown.

a phloem cell-specific Fe^{2+} efflux may affect the specificity of NH_4^+ -induced Fe deposition in the phloem. A comprehensive map of the microarray expression profiles of root cell types showed that *FPN1* is mainly expressed in phloem cells⁴⁵. Therefore, the Fe^{2+} efflux protein *FPN1* may also play a role in controlling the phloem specificity of Fe deposition. Nevertheless, disruption of *FPN1* in T-DNA *fpn1* insertion mutants did not improve PR growth under NH_4^+ stress as it did in *lpr2* mutants (Supplementary Fig. 25), refuting the above-assumed role of *FPN1*. Another possible mechanism is that the allocation of photosynthesis products via phloem may allow the cell wall matrix of phloem cells and their adjacent cells to accumulate greater reductants, which favors producing Fe^{2+} for LPR2-catalyzed reactions. Regardless of the origin of Fe^{2+} in the cell wall matrix of phloem, the massive Fe deposition in the phloem due to NH_4^+ stress closely depends on the action of LPR2.

Interestingly, Fe is also a key player in remodeling PR development in response to inorganic phosphate (p_i) deficiency, which mainly depends on the actions of LPR1^{23,46–50}. However, although the amino acid sequences of LPR1 and LPR2 are 79% identical²³, only LPR2 remodels PR development in the presence of NH_4^+ as the primary N source (Fig. 1). The failure to restore the NH_4^+ -sensitive phenotype in *lpr2* mutants by confining *LPR1* expression to the LPR2 action site (Fig. 2e, f) suggests that the enzymatic actions of LPR1 and LPR2 in plants may be differently regulated. Furthermore, the tissue distribution of LPR1 also differs from that of LPR2 (Fig. 4 and Supplementary Fig. 15). The above differences may explain the specificity of LPR2 in mediating NH_4^+ sensitivity of PRs. Importantly, the K_m value of recombinant GST-LPR2 ($\sim 17 \mu\text{M Fe}^{2+}$; Fig. 2d) is higher than that of LPR1 ($\sim 3 \mu\text{M Fe}^{2+}$)²⁷. This discrepancy corresponds well with the discrepancy in Fe dose requirements in regulating PR growth responses to p_i deficiency and NH_4^+ stress: 2.5 $\mu\text{M Fe}$ was sufficient for LPR1 to inhibit PR growth under p_i deficiency²⁷, but an Fe dose of more than 10 μM was required for LPR2 to inhibit PR growth under NH_4^+ stress (Fig. 3).

Fe is a co-factor for several ROS-producing enzymes, such as NADPH oxidases, cytochrome P450 enzymes, lipoxygenases, and xanthine oxidase⁵¹. Fe redox cycling is also capable of generating ROS directly via Fenton reactions⁵². Therefore, aberrant accumulation of Fe often triggers direct and indirect bursts in ROS⁵³. Regardless of the means of Fe regulation of ROS generation, our study showed a clear burst in ROS in root phloem as a result of NH_4^+ -induced Fe deposition (Fig. 5c–e). However, we were unable to distinguish whether this burst was generated in the intra- or extracellular matrix of phloem. Considering the apoplastic Fe deposition in the phloem, the NH_4^+ -induced burst of ROS is most likely an extracellular process. Studies have revealed a strong connection between callose deposition and bursts of ROS in response to external biotic and abiotic cues³³. The ROS burst is also responsible for the induction of callose deposition in response to NH_4^+ stress (Fig. 6d). The p_i deficiency-induced PR growth inhibition was identified to be associated with enhanced

callose accumulations in the elongation zone and SCN, which mainly depends on LPR1-mediated Fe deposition^{26,47}. Unexpectedly, our study showed that although Fe deposition was also observed in the SCN in all treatments, particularly under Fe^{low} conditions, the callose in this region did not accumulate correspondingly across the treatments (Figs. 3c and 6a). Callose is degraded by β -1,3-glucanases⁵⁴. Bioinformatic analyses have identified approximately 50 β -1,3-glucanase-related genes in Arabidopsis⁵⁵. A recent single-cell RNA-Seq showed that several β -1,3-glucanase-related genes, such as *At1g66250*, *At2g05790*, *At2g01630* (*PdBG2*), *At4g29360*, *At5g42100*, and *At5g58090*, are preferentially expressed in root SCN⁵⁶. The impacts of these β -1,3-glucanases in callose accumulation in the SCN may vary in different treatments.

The phloem is implicated as an important mediator of plant growth plasticity in response to environmental cues⁵⁷. Under normal growth conditions, callose is present in the sieve plates and plasmodesmata neck region of phloem at a basal level. Heavy deposition of callose in the phloem may plug sieve pores and decrease plasmodesmal permeability^{54,58}. Indeed, our phloem-mobile probe test using esculin provides direct evidence that NH_4^+ -induced callose deposition significantly inhibits phloem transport and unloading. Sucrose is the major transport sugar in the phloem from cotyledon or mature leaves to roots, while root growth depends highly on the sucrose imported from shoot parts⁵⁷. Esculin is loaded into the phloem in a strict sucrose transporter-dependent manner^{35,38}. Therefore, the NH_4^+ -induced inhibition of phloem action, as indicated by esculin (Fig. 7a, b), suggests that the sucrose supply to the root growth zone may be insufficient for sustaining normal cell division and differentiation. This idea is supported by the finding that elevation of sucrose supplementation in the upper part of detached roots completely rescued PR growth under NH_4^+ stress (Fig. 7c). Previously, several physiological issues, including depletion of the carbon supply, deficiency of mineral cations (i.e., K^+), excess root energy demands associated with NH_4^+ assimilation, and high energetic cost due to futile transmembrane NH_4^+ cycling, were proposed as toxic actions of NH_4^+ ^{1,59}. However, these actions may be related to the inhibition of sucrose transport in the phloem due to aberrant Fe deposition. This is because insufficient sucrose supply would not only directly lead to carbon depletion but also result in failure to meet the energy demands for either excess NH_4^+ assimilation or futile transmembrane NH_4^+ cycling. In addition, the sucrose loading into phloem requires the action of K^+ loading⁶⁰, and thus a deficiency of K^+ caused by NH_4^+ stress could further result in inhibition of sucrose transport in the phloem. Within these contexts, inhibition of phloem action as a consequence of Fe deposition could be a primary mechanism that connects the inhibition of root development to NH_4^+ stress.

It is worth noting that, in addition to transporting sugar, phloem also delivers other numerous substances, including proteins, RNAs, and peptides, but currently, only a few have been confirmed to be associated with a function⁶¹. Recently, the

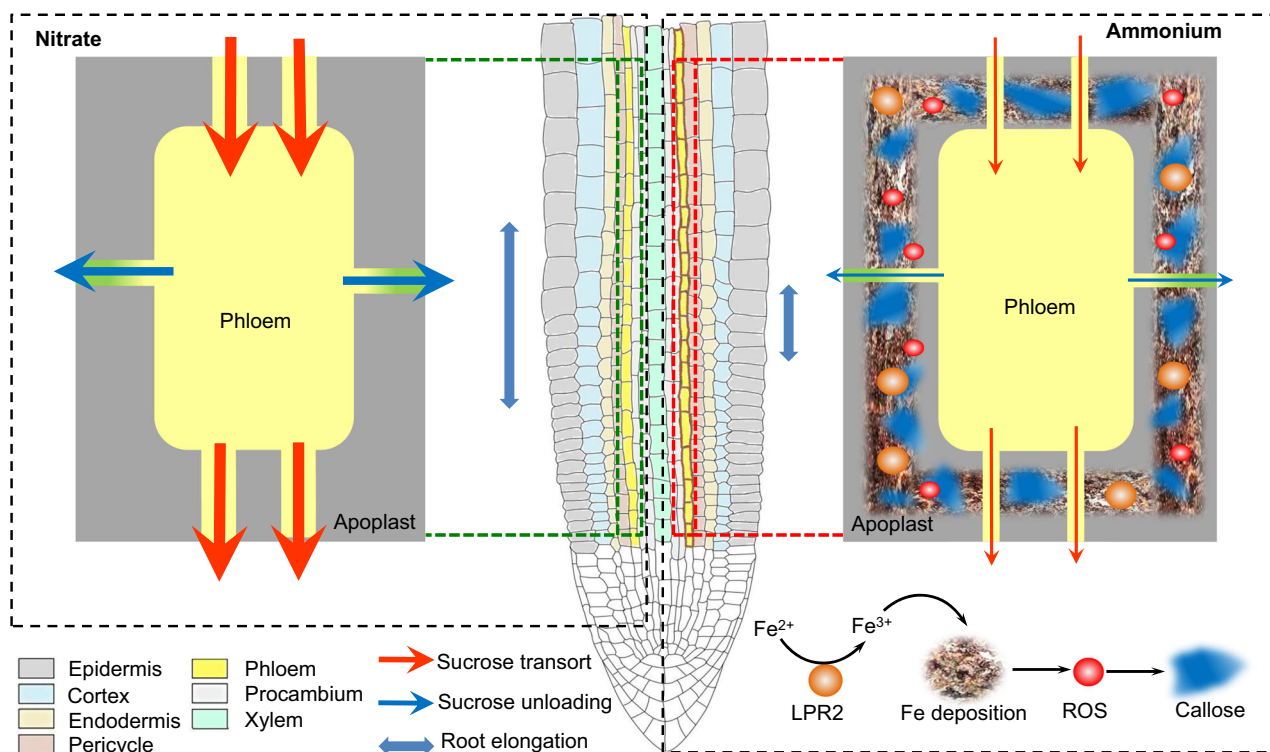


Fig. 8 Schematic model of the mechanism that connects remodeling of root development to NH_4^+ as the primary N source. In comparison with NO_3^- as the primary N source, NH_4^+ supplementation as the predominant N source induces excessive Fe deposits in the apoplast of root phloem via a catalytic reaction of Fe^{2+} oxidation to Fe^{3+} , which depends on the action of the cell wall-localized ferroxidase LPR2 in root stele. Such an aberrant Fe accumulation then inhibits phloem transport and unloading by triggering a burst of reactive oxygen species, which subsequently induces massive callose deposition. Consequently, sucrose is insufficiently allocated to the root growth zone, which arrests root development.

movement of 5-methylcytosine-modified AtTCTP1 mRNA in the phloem was shown to slightly promote PR growth of Arabidopsis⁶². In addition, the protophloem has been proposed as a nexus that senses CLE peptides that convey environmental conditions and adjusts root growth accordingly⁶³. In these contexts, the action of phloem in regulating PR growth is not merely limited to the movement of sucrose. Therefore, the roles of other substances, particularly signal molecules, in the regulation of PR growth inhibition from a resulting impairment of phloem action under NH_4^+ stress might merit further study.

In conclusion, we propose a mechanism by which root development is remodeled in response to a variation in the predominant N source (Fig. 8). In comparison with NO_3^- as the major N source, NH_4^+ induces excessive Fe deposits in the apoplast of root phloem via the action of cell wall-localized ferroxidase LPR2, which catalyzes the oxidation of Fe^{2+} into Fe^{3+} . Such an aberrant Fe accumulation triggers ROS generation and consequently leads to massive callose deposition. This impairs phloem action and arrests root development because of insufficient sucrose allocation to the root growth zone. Our findings may provide a strategy for improving plant adaptation to NH_4^+ -rich soil environments via biotechnological pathways to manipulate Fe deposition in root phloem.

Methods

Plant lines and growth conditions. Wild-type *A. thaliana* accession Columbia (Col-0) was used as a control for all experiments. The T-DNA insertion lines *lpr2-1* (SALK_091930), *isas* (SALK_056696), and *fpn1* (SALK_055499) were obtained from the Arabidopsis Biological Resource Center (Ohio State University, Columbus, OH, USA). The *lpr1-1* and *lpr1-1lpr2-1* (*lpr1lpr2*) mutants were provided by Prof Liu Dong (Tsinghua University, Beijing, China); *pSUC2::GFP-sporamin* and *roGFP2-orp1* were provided by Prof Chun-Ming Liu (Chinese Academy of Sciences, Beijing, China) and Dr Markus Schwarzländer (University of Münster,

Münster, Germany), respectively. Homozygous lines were used in this study, and the insertions were verified using the primers listed in Supplementary Data 2.

The plants were grown on a basic agar medium in sterile Petri dishes. Briefly, the seeds were surface-sterilized using 25% NaClO and sown on basal medium containing 1% (w/v) sucrose, 0.8% (w/v) agar, and MES. The nutrient composition of the basal medium was as follows: 3 mM KNO_3 , 0.5 mM $(\text{NH}_4)_2\text{SO}_4$, 1 mM CaCl_2 , 500 μM NaH_2PO_4 , 500 μM MgSO_4 , 100 μM Fe(II)-EDTA , 10 μM H_3BO_3 , 0.5 μM ZnSO_4 , 0.5 μM MnSO_4 , 0.1 μM $(\text{NH}_4)_6\text{Mo}_7\text{O}_{24}$, and 0.1 μM CuSO_4 (pH 5.7). After vernalization at 4 °C for 2 days, the Petri dishes were moved to a controlled-environment growth chamber with a 12 h light/12 h dark cycle at 22 °C. The 4-day-old seedlings were then transferred to basic agar media with 2.5 mM $(\text{NH}_4)_2\text{SO}_4$ or 5 mM KNO_3 as the sole N source, containing various doses of Fe(II)-EDTA as indicated in the figure legends. The resulting differences in K concentrations were balanced by adjusting the KCl concentration. To avoid a possible artificial impact from light irradiation on roots, the roots of seedlings were covered with a sterile black plastic sheet, as depicted in Supplementary Fig. 3a.

Generation of transgenic plants. For the generation of plant expression vectors for genetic complementation, the 5949-bp genomic DNA of *LPR2* (including a 2928-bp region upstream of the start codon) and the 4262-bp genomic DNA of *LPR1* (including a 2178-bp region upstream of the start codon) were cloned into a pEarleyGate 101 vector containing a YFP reporter. The resulting constructs *pLPR2::LPR2-YFP* and *pLPR1::LPR1-YFP* were then transformed into *lpr2-1* and *lpr1-1* mutants, respectively, to generate complementation lines (*pLPR2::LPR2-YFP/lpr2-1* and *pLPR1::LPR1-YFP/lpr1-1*, respectively). For analysis of subcellular localization of LPR2, the *LPR2* coding sequence (CDS), fused to GFP, was cloned into a modified pCambia1300 vector containing a doubled CaMV 35S promoter. The resulting construct was transformed into Col-0 to obtain the *p35S::LPR2-GFP* line. For the *LPR2* promoter-confined complementation assay of *LPR1*, the 2928-bp region upstream of the start codon of *LPR2*, together with either the CDS or genomic sequence of *LPR1*, was cloned into a pCambia1300 vector. The resulting construct was transformed into *lpr2-1* mutants to generate *pLPR2::LPR1^{CDS}/lpr2-1* or *pLPR2::LPR1^{genomic}/lpr2-1* transformants.

All primers used for vector construction are listed in Supplementary Data 2. All transgenic lines were generated by agrobacterium-mediated transformation using the floral dip method. Only homozygous lines were used in this study.

Measurements of root meristem size and cell elongation. Measurements of root meristem size and cell elongation were performed 4 days after seedling transfer to

the indicated media. The roots were incubated in $10 \mu\text{g mL}^{-1}$ propidium iodide (PI; Sigma-Aldrich, St. Louis, MO, USA) in the dark for 5 min and rinsed twice with deionized water. The roots were then imaged by confocal microscopy. Root meristem size was measured as the number of cortical cells between the quiescent center and the first elongated cell (Supplementary Fig. 3b). The average number of elongating cells in the same cell file was calculated from the first elongating cell to the first differentiating cell. The length of the latter cell type was measured to calculate the average length of the first differentiating cells.

Histochemical Fe staining. The histochemical Fe staining of roots was adapted from the method of Roschztardt et al.²². Briefly, after 4 days of treatments in the indicated media, the roots were incubated for 45 min under vacuum (500 mbar) with Perls' staining solution (2% [v/v] HCl and 2% [w/v] potassium ferrocyanide). After being rinsed three times with deionized water, the root samples were incubated for 1 h in a methanol solution containing 10 mM NaN_3 and 0.3% H_2O_2 . Subsequently, the root samples were washed with 100 mM Na-phosphate buffer (pH 7.4) and intensified by 5 min incubation in the same buffer containing 0.025% (v/v) DAB and 0.005% (v/v) H_2O_2 . The reaction was stopped by washing with deionized water and optically cleared with chloral hydrate. Stained root samples were observed using a differential interference contrast microscope (Nikon, Tokyo, Japan).

Confocal microscopy and staining procedures. Confocal analyses were performed on either an Olympus FV3000 (Tokyo, Japan) or a Zeiss LSM 880 microscope (Oberkochen, Germany). For callose staining, roots were incubated in 150 mM K_2HPO_4 and 0.01% (w/v) aniline blue in the dark for 2 h. For ROS staining, roots were incubated with $10 \mu\text{M}$ H_2DCFDA (Beyotime Biotech, Shanghai, China) in the dark for 30 min and then washed twice with deionized water. For PI or FM4-64 staining, roots were directly imaged in $10 \mu\text{M}$ PI or $4 \mu\text{M}$ FM4-64 (Thermo Fisher Scientific, Waltham, MA, USA). The excitation (ex)/emission (em) parameters for confocal analyses are as follows: GFP/YFP/ H_2CDFDA ex: 488 nm, em: 500–550 nm; PI/FM4-64 ex: 561, em: 570–670 nm; aniline blue ex: 405 nm, em: 475–525 nm; esculin ex: 405 nm, em: 420–480 nm; and rGFP2-Orp1 ex: 405 and 488 nm in sequence, em: 505–535 nm and 425–475 nm (auto fluorescence recorded at ex: 405 nm for subtraction in calculating the ratio 405/488 nm)²⁹.

Analysis of esculin movement. The esculin movement in the phloem of PRs was detected as described by Knox³⁶. Briefly, after 4-day treatment with the indicated media, cotyledons were pretreated with 0.3 μL 2.5% (v/v) Adigor solution (Syn-genta, Basel, Switzerland) for 1 h and subsequently supplemented with 0.5 μL 9 mg mL^{-1} esculin solution. After 10 min, the appearance of esculin in the phloem of the PR was noted. Then, the fluorescent front in root phloem was marked on the plate, and the time was noted. Thereafter, the fluorescence in root phloem was rechecked after 10 min, and the new front was marked along with the time. The distance of esculin movement in the phloem was taken as the length between the two marks. The PTV was calculated from the distance and the interval time. In addition, once esculin was imported into the root tip, individual images, with their times of acquisition, were recorded to evaluate the unloading of the phloem unloading³⁷.

In vitro ferroxidase characterization of recombinant proteins. The *LPR2* CDS without signal peptide sequences were cloned into pGEX-6P-1, which enables the fusion of a GST tag. Isopropyl β -D-1 thiogalactopyranoside (0.5 mM) was supplied to *Escherichia coli* strain Arctic Express carrying pGEX-6P-1 or pGEX-6P-1-LPR2 at 14 °C for 20 h to induce expression of the GST or GST-LPR2. The cells were harvested by centrifugation ($4000 \times g$, 30 min, 4 °C) and lysed in extraction buffer (50 mM Tris-HCl (pH 7.4), 150 mM NaCl, 1 mM PMSF, and 100 $\mu\text{g mL}^{-1}$ mL lysozyme) with sonication. After centrifugation at $15,000 \times g$ at 4 °C for 30 min, the supernatant was recovered, then the GST or GST-LPR2 protein was purified using a column containing Glutathione Sepharose 4B beads (Solarbio, Beijing, China)⁶⁴. The purified proteins were further desalted and concentrated using centrifugal filter (Merck Millipore, Amicon Ultra 15, molecular weight cut-off of 10 kDa).

Ferroxidase activity was measured using a ferrozine-based method²⁶. Briefly, a defined amount of protein was mixed with various amounts of ferrous ammonium sulfate in a solution of 0.1 M sodium acetate with 100 μM CuSO_4 (pH 5.0) to reach desired substrate concentrations. After incubation, 200- μL samples were taken in appropriate intervals and transferred to 96-well plates for reaction-quenching with 14 μL 18 mM ferrozine. The absorbance at 560 nm was measured using a plate reader (SpectraMax i3x; Molecular Devices, San Jose, CA, USA). The decrease in the substrate was then used to calculate the oxidation of Fe^{2+} . The K_m and V_{max} were calculated using the Michaelis–Monod model in GraphPad Prism 8 software (GraphPad Software, San Diego, CA, USA).

Determination of ammonium. Root samples were ground in liquid N_2 immediately after collection. One milliliter of 0.3 M sulfuric acid solution was added to the frozen powder, followed by vortexing. The mixture was centrifuged at $12,000 \times g$ at 4 °C for 10 min. The NH_4^+ concentration in the supernatant was determined colorimetrically using a method based on the phenol-hypochlorite assay at 635 nm in a spectrophotometer¹⁰.

Quantitative real-time RT-PCR. After 4-day treatment in the indicated media, the total RNA in roots was extracted using RNAisoPlus (Takara, Kyoto, Japan) and treated with DNase I to remove contaminant genomic DNA. We synthesized cDNA using a PrimeScript RT reagent kit (Takara) according to the manufacturer's protocol. We performed qRT-PCR analysis of *LPR2* with TB Green Premix Ex Taq II (Takara) on a Step One system (Agilent Technologies, Santa Clara, CA, USA). The primers used for qRT-PCR analysis are listed in Supplementary Data 2. *UBQ10* and *EF1 α* were used as the reference genes. Relative transcript abundances were determined by normalizing to the geometric mean of expression of two reference genes for each sample⁶⁵.

Immunoblot analysis. Polyclonal LPR2 epitope-specific antibody was raised in rabbits against a synthetic peptide (LPR2:DEGGIKQEERLFLNGLKLE-C) and affinity-purified (ABclonal, Wuhan, China). After 4-day treatment in the indicated media, the total root proteins were extracted using a Plant Protein Extraction Kit (Solarbio, Beijing, China) following the manufacturer's protocol. The protein samples were separated in 10% SDS/PAGE gels and transferred to nitrocellulose membranes (Bio-Rad, Hercules, CA, USA) in semi-dry conditions (Trans-Blot SD semi-dry transfer cell; Bio-Rad). The membranes were incubated in blocking buffer (TBST, 5% milk powder) at room temperature for 2 h and then incubated overnight in blocking buffer containing anti-LPR2 antibody (1:2000), rabbit polyclonal anti-GFP (1:5000; catalogue no. AE011, ABclonal, Wuhan, China) or mouse monoclonal anti-actin antibody (1:2000; catalogue no. D191048, Sangon Biotech, Shanghai, China) at 4 °C. HRP-conjugated goat anti-rabbit IgG (1:5000; catalogue no. D1110058, Sangon Biotech) or goat anti-mouse IgG (1:5000, catalogue no. D1110087, Sangon Biotech) was used as a secondary antibody. The signal was detected using an ECL Kit (Tanon™; AbClon). In addition, the membranes were also stained with Ponceau S to visualize total proteins as the loading reference.

RNA sequencing and GO analysis. After 4-day treatment in the indicated media, the total RNA was extracted from the roots of Col-0 and *lpr2-1* seedlings using MagZol Reagent (Magen, Guangzhou, China) following the manufacturer's protocol. We constructed mRNA-Seq libraries using NEBNext Ultra RNA Library Prep Kit for Illumina (NEB, Ipswich, MA, USA). The quality of the libraries was assessed using an Agilent 2100 Bioanalyzer. Sequencing was performed using a HiSeq Xten sequencer (Illumina, San Diego, CA, USA) at RIBOBIO (Guangzhou, China). Raw reads were quality controlled and trimmed using FastQC v0.11.8 (<http://www.bioinformatics.babraham.ac.uk/projects/fastqc/>) and Trimmomatic. The clean reads were mapped to the Arabidopsis genome (TAIR10) using HISAT2 and a GTF annotation file from the Ensembl Plants database (<ftp://ftp.ensemblgenomes.org>) and then analyzed using *Stringtie* and *ballgown*⁶⁶. Significant DEGs were assessed using a *P* value threshold of <0.05 and $|\log_2(\text{fold change})| > 1$ using DEGseq⁶⁷. GO term enrichment analysis was performed with R packages clusterProfiler and database.org.At.tair.db (version 3.13.0)⁶⁸.

Statistical analyses. Data were analyzed by one-way and two-way ANOVA with post-hoc Tukey HSD test using Prism v8 (GraphPad). A *P* value < 0.05 was considered statistically significant.

Reporting summary. Further information on research design is available in the Nature Research Reporting Summary linked to this article.

Data availability

Data supporting the findings of this work are available within the paper and its Supplementary Information files. A reporting summary for this article is available as a Supplementary Information file. RNA-seq raw data were deposited in NCBI's SRA (Sequence Read Archive) under the accession number PRJNA789742. Source Data are provided with this paper.

Received: 17 June 2021; Accepted: 10 January 2022;

Published online: 28 January 2022

References

- Britto, D. T. & Kronzucker, H. J. NH_4^+ toxicity in higher plants: a critical review. *J. Plant Physiol.* **159**, 567–584 (2002).
- Nakamura, T. & Nakamura, M. Ecophysiological mechanisms characterising fen and bog species: focus on variations in nitrogen uptake traits under different soil–water pH. *Oecologia* **168**, 913–921 (2012).
- Britto, D. T. & Kronzucker, H. J. Ecological significance and complexity of N-source preference in plants. *Ann. Bot.* **112**, 957–963 (2013).
- Esteban, R., Ariz, I., Cruz, C. & Moran, J. F. Mechanisms of ammonium toxicity and the quest for tolerance. *Plant Sci.* **248**, 92–101 (2016).
- Li, Y., Zhou, J., Hao, D., Yang, S. & Su, Y. Arabidopsis under ammonium over-supply: characteristics of ammonium toxicity in relation to the activity of ammonium transporters. *Pedosphere* **30**, 314–325 (2020).

6. Li, B., Li, G., Kronzucker, H. J., Baluška, F. & Shi, W. Ammonium stress in Arabidopsis: signaling, genetic loci, and physiological targets. *Trends Plant Sci.* **19**, 107–114 (2014).
7. Rogato, A. et al. Characterization of a developmental root response caused by external ammonium supply in *Lotus japonicus*. *Plant Physiol.* **154**, 784–795 (2010).
8. Yuan, L. et al. The organization of high-affinity ammonium uptake in Arabidopsis roots depends on the spatial arrangement and biochemical properties of AMT1-type transporters. *Plant Cell* **19**, 2636–2652 (2007).
9. Straub, T., Ludewig, U. & Neuhäuser, B. The kinase CIPK23 inhibits ammonium transport in *Arabidopsis thaliana*. *Plant Cell* **29**, 409–422 (2017).
10. Tian, W. H. et al. A transcription factor STOP1-centered pathway coordinates ammonium and phosphate acquisition in Arabidopsis. *Mol. Plant* **14**, 1554–1568 (2021).
11. Zhu, Y. et al. Adaptation of plasma membrane H⁺-ATPase of rice roots to low pH as related to ammonium nutrition. *Plant Cell Environ.* **32**, 1428–1440 (2009).
12. Weng, L. et al. Potassium alleviates ammonium toxicity in rice by reducing its uptake through activation of plasma membrane H⁺-ATPase to enhance proton extrusion. *Plant Physiol. Biochem.* **151**, 429–437 (2020).
13. Sun, D. et al. Kinase SnRK1.1 regulates nitrate channel SLAH3 engaged in nitrate-dependent alleviation of ammonium toxicity. *Plant Physiol.* **186**, 731–749 (2021).
14. Hachiya, T. et al. Excessive ammonium assimilation by plastidic glutamine synthetase causes ammonium toxicity in *Arabidopsis thaliana*. *Nat. Commun.* **12**, 1–10 (2021).
15. Jian, S. et al. NRT1.1-related NH₄⁺ toxicity is associated with a disturbed balance between NH₄⁺ uptake and assimilation. *Plant Physiol.* **178**, 1473–1488 (2018).
16. Li, G. et al. The Arabidopsis AMOT1/EIN3 gene plays an important role in the amelioration of ammonium toxicity. *J. Exp. Bot.* **70**, 1375–1388 (2019).
17. Qin, C. et al. GDP-mannose pyrophosphorylase is a genetic determinant of ammonium sensitivity in *Arabidopsis thaliana*. *Proc. Natl Acad. Sci. USA* **105**, 18308–18313 (2008).
18. Cao, Y., Glass, A. D. & Crawford, N. M. Ammonium inhibition of Arabidopsis root growth can be reversed by potassium and by auxin resistance mutations *aux1*, *axr1*, and *axr2*. *Plant Physiol.* **102**, 983–989 (1993).
19. Liu, Y., Lai, N., Gao, K., Chen, F., Yuan, L. & Mi, G. Ammonium inhibits primary root growth by reducing the length of meristem and elongation zone and decreasing elemental expansion rate in the root apex in *Arabidopsis thaliana*. *PLoS One* **8**, e61031 (2013).
20. Zheng, Z., Wang, Z., Wang, X. & Liu, D. Blue light-triggered chemical reactions underlie phosphate deficiency-induced inhibition of root elongation of Arabidopsis seedlings grown in Petri dishes. *Mol. Plant* **12**, 1515–1523 (2019).
21. Liu, Z., Giehl, R. F. H., Bienert, M. D., von Wirén, N. & Bienert, G. P. Light-triggered reactions do not bias boron deficiency-induced root inhibition of Arabidopsis seedlings grown in petri dishes. *Mol. Plant* **14**, 1211–1214 (2021).
22. Alonso, J. M. et al. Genome-wide insertional mutagenesis of *Arabidopsis thaliana*. *Science* **301**, 653–657 (2003).
23. Svistoonoff, S. et al. Root tip contact with low-phosphate media reprograms plant root architecture. *Nat. Genet.* **39**, 792–796 (2007).
24. Beemster, G. T. & Baskin, T. I. Analysis of cell division and elongation underlying the developmental acceleration of root growth in *Arabidopsis thaliana*. *Plant Physiol.* **116**, 1515–1526 (1998).
25. Armenteros, J. J. A. et al. SignalP 5.0 improves signal peptide predictions using deep neural networks. *Nat. Biotechnol.* **37**, 420–423 (2019).
26. Müller, J. et al. Iron-dependent callose deposition adjusts root meristem maintenance to phosphate availability. *Dev. Cell* **33**, 216–230 (2015).
27. Naumann, C. et al. Bacterial-type plant ferroxidases tune local phosphate sensing in root development. *bioRxiv*. Preprint at <https://doi.org/10.1101/2021.03.19.436157> (2021).
28. Roschzttardtz, H., Conéjéro, G., Curie, C. & Mari, S. Identification of the endodermal vacuole as the iron storage compartment in the Arabidopsis embryo. *Plant Physiol.* **151**, 1329–1338 (2009).
29. Nietzel, T. et al. The fluorescent protein sensor roGFP2-Orp1 monitors in vivo H₂O₂ and thiol redox integration and elucidates intracellular H₂O₂ dynamics during elicitor-induced oxidative burst in *Arabidopsis*. *N. Phytol.* **221**, 1649–1664 (2019).
30. Rodrigues, O. et al. Aquaporins facilitate hydrogen peroxide entry into guard cells to mediate ABA- and pathogen-triggered stomatal closure. *Proc. Natl Acad. Sci. USA* **114**, 9200–9205 (2017).
31. Bestetti, S. et al. A persulfidation-based mechanism controls aquaporin-8 conductance. *Sci. Adv.* **4**, earr5770 (2018).
32. Shen, Z. et al. Fe-based carbonitride as Fenton-like catalyst for the elimination of organic contaminants. *Environ. Res.* **198**, 110486 (2021).
33. Castro, B. et al. Stress-induced reactive oxygen species compartmentalization, perception and signalling. *Nat. Plants* **7**, 403–412 (2021).
34. Stadler, R. et al. Expression of GFP-fusions in Arabidopsis companion cells reveals non-specific protein trafficking into sieve elements and identifies a novel post-phloem domain in roots. *Plant J.* **41**, 319–331 (2005).
35. Knoblauch, M. et al. Multispectral phloem-mobile probes: properties and applications. *Plant Physiol.* **167**, 1211–1220 (2015).
36. Knox, K. Measuring phloem transport velocity in Arabidopsis seedlings using the fluorescent coumarin glucoside, esculin. In: *Phloem* (ed. Liesche J.) (Humana, New York, NY, 2019).
37. Oparka, K. J., Duckett, C. M., Prior, D. A. M. & Fisher, D. B. Real-time imaging of phloem unloading in the root tip of Arabidopsis. *Plant J.* **6**, 759–766 (1994).
38. Gora, P. J., Reinders, A. & Ward, J. M. A novel fluorescent assay for sucrose transporters. *Plant Methods* **8**, 1–6 (2012).
39. Xu, G., Fan, X. & Miller, A. J. Plant nitrogen assimilation and use efficiency. *Annu. Rev. Plant Biol.* **63**, 153–182 (2012).
40. Wang, P. Friend or foe: how nitrate antagonizes ammonium toxicity. *Plant Physiol.* **186**, 210–211 (2021).
41. Motomura, S. The relationship between ferrous iron formation and nitrogen metabolism in soil. *Soil Sci. Plant Nutr.* **8**, 9–17 (1962).
42. Ponnampерuma, F. N. The chemistry of submerged soils. In: *Advances in Agronomy* (ed. Brady N. C.) (Academic Press, London, 1972).
43. Li, Y., Chapman, S. J., Nicol, G. W. & Yao, H. Nitrification and nitrifiers in acidic soils. *Soil Biol. Biochem.* **116**, 290–301 (2018).
44. Ifansyah, H. Soil pH and solubility of aluminum, iron, and phosphorus in Ultisols: the roles of humic acid. *J. Trop. Soils* **18**, 203–208 (2014).
45. Brady, S. M. et al. A high-resolution root spatiotemporal map reveals dominant expression patterns. *Science* **318**, 801–806 (2007).
46. Ward, J. T., Lahner, B., Yakubova, E., Salt, D. E. & Raghothama, K. G. The effect of iron on the primary root elongation of Arabidopsis during phosphate deficiency. *Plant Physiol.* **147**, 1181–1191 (2008).
47. Balzergue, C. et al. Low phosphate activates STOP1-ALMT1 to rapidly inhibit root cell elongation. *Nat. Commun.* **8**, 1–16 (2017).
48. Dong, J. et al. An Arabidopsis ABC transporter mediates phosphate deficiency-induced remodeling of root architecture by modulating iron homeostasis in roots. *Mol. Plant* **10**, 244–259 (2017).
49. Mora-Macias, J. et al. Malate-dependent Fe accumulation is a critical checkpoint in the root developmental response to low phosphate. *Proc. Natl Acad. Sci. USA* **114**, E3563–E3572 (2017).
50. Gao, Y. Q. et al. Long-distance blue light signalling regulates phosphate deficiency-induced primary root growth inhibition. *Mol. Plant* **14**, 1539–1553 (2021).
51. Dixon, S. J. & Stockwell, B. R. The role of iron and reactive oxygen species in cell death. *Nat. Chem. Biol.* **10**, 9–17 (2014).
52. Kosman, D. J. Redox cycling in iron uptake, efflux, and trafficking. *J. Biol. Chem.* **285**, 26729–26735 (2010).
53. Distéfano, A. M. et al. Ferroptosis in plants: triggers, proposed mechanisms, and the role of iron in modulating cell death. *J. Exp. Bot.* **72**, 2125–2135 (2021).
54. Wu, S. W., Kumar, R., Iswanto, A. B. B. & Kim, J. Y. Callose balancing at plasmodesmata. *J. Exp. Bot.* **69**, 5325–5339 (2018).
55. Doxey, A. C., Yaish, M. W., Moffatt, B. A., Griffith, M. & McConkey, B. J. Functional divergence in the Arabidopsis β-1, 3-glucanase gene family inferred by phylogenetic reconstruction of expression states. *Mol. Biol. Evol.* **24**, 1045–1055 (2007).
56. Denyer, T. et al. Spatiotemporal developmental trajectories in the Arabidopsis root revealed using high-throughput single-cell RNA sequencing. *Dev. Cell* **48**, 840–852 (2019).
57. López-Salmerón, V., Cho, H., Tonn, N. & Greb, T. The phloem as a mediator of plant growth plasticity. *Curr. Biol.* **29**, R173–R181 (2019).
58. Wang, Y., Li, X., Fan, B., Zhu, C. & Chen, Z. Regulation and function of defense-related callose deposition in plants. *Int. J. Mol. Sci.* **22**, 2393 (2021).
59. Bittsánszky, A., Pilinszky, K., Gyulai, G. & Komives, T. Overcoming ammonium toxicity. *Plant Sci.* **231**, 184–190 (2015).
60. Wang, Y., Chen, Y. F. & Wu, W. H. Potassium and phosphorus transport and signaling in plants. *J. Integr. Plant Biol.* **63**, 34–52 (2021).
61. Koenig, A. M. & Hoffmann-Benning, S. The interplay of phloem-mobile signals in plant development and stress response. *Biosci. Rep.* **40**, BSR20193329 (2020).
62. Yang, L. et al. m5C methylation guides systemic transport of messenger RNA over graft junctions in plants. *Curr. Biol.* **29**, 2465–2476 (2019).
63. Anne, P. & Hardtke, C. S. Phloem function and development-biophysics meets genetics. *Curr. Opin. Plant Biol.* **43**, 22–28 (2018).
64. Ma, J. et al. SARS-CoV-2 nucleocapsid suppresses host pyroptosis by blocking Gasdermin D cleavage. *EMBO J.* **40**, e108249 (2021).
65. Vandesompele, J. et al. Accurate normalization of real-time quantitative RT-PCR data by geometric averaging of multiple internal control genes. *Genome Biol.* **3**, 1–12 (2002).

66. Pertea, M., Kim, D., Pertea, G. M., Leek, J. T. & Salzberg, S. L. Transcript-level expression analysis of RNA-seq experiments with HISAT, StringTie and Ballgown. *Nat. Protoc.* **11**, 1650–1667 (2016).
67. Wang, L., Feng, Z., Wang, X., Wang, X. & Zhang, X. DEGseq: an R package for identifying differentially expressed genes from RNA-seq data. *Bioinformatics* **26**, 136–138 (2010).
68. Yu, G., Wang, L. G., Han, Y. & He, Q. Y. clusterProfiler: an R package for comparing biological themes among gene clusters. *OMICS* **16**, 284–287 (2012).

Acknowledgements

This work was supported by Natural Science Foundation of China [31670258 and 32100232] and the Zhejiang Province Natural Science Foundation (grant no. LZ21D010001). We are deeply grateful Dr Zachary Nimchuk, Prof Liu Dong, and Prof Chun-Ming Liu for providing seeds. Dr Liang Ni (AES of Zhejiang University) is gratefully acknowledged for his assistance in seed propagation. We would like to thank Editage (www.editage.cn) for English language editing.

Author contributions

C.W.J. conceived the project. X.X.L. performed the majority of experiments. H.H.Z., Q.Y.Z., J.Y.Y., Y.X.Z., M.Z., and X.T.J. assisted in performing the experiments and analyzing the data. W.X.D. performed bioinformatic analyses. X.X.L. and C.W.J. interpreted the data, generated the figures, and wrote the manuscript. S.J.Z. and X.Y.L. provided suggestions and revised the manuscript.

Competing interests

The authors declare no competing interests.

Additional information

Supplementary information The online version contains supplementary material available at <https://doi.org/10.1038/s41467-022-28261-4>.

Correspondence and requests for materials should be addressed to Chong Wei Jin.

Peer review information *Nature Communications* thanks Joerg Ziegler and the other, anonymous, reviewer(s) for their contribution to the peer review of this work. Peer reviewer reports are available.

Reprints and permission information is available at <http://www.nature.com/reprints>

Publisher's note Springer Nature remains neutral with regard to jurisdictional claims in published maps and institutional affiliations.



Open Access This article is licensed under a Creative Commons Attribution 4.0 International License, which permits use, sharing, adaptation, distribution and reproduction in any medium or format, as long as you give appropriate credit to the original author(s) and the source, provide a link to the Creative Commons license, and indicate if changes were made. The images or other third party material in this article are included in the article's Creative Commons license, unless indicated otherwise in a credit line to the material. If material is not included in the article's Creative Commons license and your intended use is not permitted by statutory regulation or exceeds the permitted use, you will need to obtain permission directly from the copyright holder. To view a copy of this license, visit <http://creativecommons.org/licenses/by/4.0/>.

© The Author(s) 2022